

# Cosmogenic Backgrounds to $0\nu\beta\beta$ in EXO-200

J.B. Albert,<sup>a,1</sup> D.J. Auty,<sup>b,2</sup> P.S. Barbeau,<sup>c</sup> D. Beck,<sup>d</sup> V. Belov,<sup>e</sup>  
M. Breidenbach,<sup>f</sup> T. Brunner,<sup>g,h</sup> A. Burenkov,<sup>e</sup> G.F. Cao,<sup>i</sup>  
C. Chambers,<sup>j</sup> B. Cleveland,<sup>k,3</sup> M. Coon,<sup>d</sup> A. Craycraft,<sup>j</sup>  
T. Daniels,<sup>f</sup> M. Danilov,<sup>e</sup> S.J. Daugherty,<sup>a</sup> J. Davis,<sup>f</sup>  
S. Delaquis,<sup>l</sup> A. Der Mesrobian-Kabakian,<sup>k</sup> R. DeVoe,<sup>m</sup>  
T. Didberidze,<sup>b</sup> J. Dilling,<sup>h</sup> A. Dolgolenko,<sup>e</sup> M.J. Dolinski,<sup>n</sup>  
M. Dunford,<sup>o</sup> W. Fairbank Jr.,<sup>j</sup> J. Farine,<sup>k</sup> W. Feldmeier,<sup>p</sup>  
S. Feyzbakhsh,<sup>q</sup> P. Fierlinger,<sup>p</sup> D. Fudenberg,<sup>m</sup> R. Gornea,<sup>o,h</sup>  
K. Graham,<sup>o</sup> G. Gratta,<sup>m</sup> C. Hall,<sup>r</sup> S. Herrin,<sup>f</sup> M. Hughes,<sup>b</sup>  
M.J. Jewell,<sup>m</sup> A. Johnson,<sup>f</sup> T.N. Johnson,<sup>a</sup> S. Johnston,<sup>q</sup>  
A. Karelin,<sup>e</sup> L.J. Kaufman,<sup>a</sup> R. Killick,<sup>o</sup> T. Koffas,<sup>o</sup> S. Kravitz,<sup>m</sup>  
R. Krücken,<sup>h</sup> A. Kuchenkov,<sup>e</sup> K.S. Kumar,<sup>s</sup> D.S. Leonard,<sup>t</sup>  
C. Licciardi,<sup>o</sup> Y.H. Lin,<sup>n</sup> J. Ling,<sup>d,4</sup> R. MacLellan,<sup>u</sup>  
M.G. Marino,<sup>p</sup> B. Mong,<sup>f</sup> D. Moore,<sup>m</sup> O. Njoya,<sup>s</sup> R. Nelson,<sup>v</sup>  
A. Odian,<sup>f</sup> I. Ostrovskiy,<sup>m</sup> A. Piepke,<sup>b</sup> A. Pocar,<sup>q</sup>  
C.Y. Prescott,<sup>f</sup> F. Retière,<sup>h</sup> P.C. Rowson,<sup>f</sup> J.J. Russell,<sup>f</sup>  
A. Schubert,<sup>m</sup> D. Sinclair,<sup>o,h</sup> E. Smith,<sup>n</sup> V. Stekhanov,<sup>e</sup>  
M. Tarka,<sup>s</sup> T. Tolba,<sup>l,5</sup> R. Tsang,<sup>b</sup> K. Twelker,<sup>m</sup>  
J.-L. Vuilleumier,<sup>l</sup> A. Waite,<sup>f</sup> J. Walton,<sup>d</sup> T. Walton,<sup>j</sup>  
M. Weber,<sup>m</sup> L.J. Wen,<sup>i</sup> U. Wichoski,<sup>k</sup> J. Wood,<sup>v</sup> L. Yang,<sup>d</sup>  
Y.-R. Yen,<sup>n</sup> O.Ya. Zeldovich<sup>e</sup>

<sup>a</sup>Physics Department and CEEM, Indiana University, Bloomington, Indiana 47405, USA

<sup>b</sup>Department of Physics and Astronomy, University of Alabama, Tuscaloosa, Alabama 35487, USA

<sup>c</sup>Department of Physics, Duke University, and Triangle Universities Nuclear Laboratory (TUNL), Durham, North Carolina 27708, USA

<sup>d</sup>Physics Department, University of Illinois, Urbana-Champaign, Illinois 61801, USA

<sup>e</sup>Institute for Theoretical and Experimental Physics, Moscow, Russia

---

<sup>1</sup>Corresponding author.

<sup>2</sup>Now at University of Alberta, Edmonton, Alberta, Canada

<sup>3</sup>Also SNOLAB, Sudbury ON, Canada

<sup>4</sup>Now at Sun Yat-Sen University, Guangzhou, China

<sup>5</sup>Now at Institute of High Energy Physics, Beijing, China

<sup>f</sup>SLAC National Accelerator Laboratory, Menlo Park, California 94025, USA  
<sup>g</sup>Physics Department, McGill University, Montreal, Quebec H3A 2T8, Canada  
<sup>h</sup>TRIUMF, Vancouver, British Columbia V6T 2A3, Canada  
<sup>i</sup>Institute of High Energy Physics, Beijing, China  
<sup>j</sup>Physics Department, Colorado State University, Fort Collins, Colorado 80523, USA  
<sup>k</sup>Department of Physics, Laurentian University, Sudbury, Ontario P3E 2C6, Canada  
<sup>l</sup>LHEP, Albert Einstein Center, University of Bern, Bern, Switzerland  
<sup>m</sup>Physics Department, Stanford University, Stanford, California 94305, USA  
<sup>n</sup>Department of Physics, Drexel University, Philadelphia, Pennsylvania 19104, USA  
<sup>o</sup>Physics Department, Carleton University, Ottawa, Ontario K1S 5B6, Canada  
<sup>p</sup>Technische Universität München, Physikdepartment and Excellence Cluster Universe, Garching 85748, Germany  
<sup>q</sup>Amherst Center for Fundamental Interactions and Physics Department, University of Massachusetts, Amherst, MA 01003, USA  
<sup>r</sup>Physics Department, University of Maryland, College Park, Maryland 20742, USA  
<sup>s</sup>Department of Physics and Astronomy, Stony Brook University, SUNY, Stony Brook, New York 11794, USA  
<sup>t</sup>IBS Center for Underground Physics, Daejeon, Korea  
<sup>u</sup>Physics Department, University of South Dakota, Vermillion, South Dakota 57069, USA  
<sup>v</sup>Waste Isolation Pilot Plant, Carlsbad, New Mexico 88220, USA

E-mail: [joalbert@indiana.edu](mailto:joalbert@indiana.edu)

**Abstract.** As neutrinoless double-beta decay experiments become more sensitive and intrinsic radioactivity in detector materials is reduced, previously minor contributions to the background must be understood and eliminated. With this in mind, cosmogenic backgrounds have been studied with the EXO-200 experiment. Using the EXO-200 TPC, the muon flux (through a flat horizontal surface) underground at the Waste Isolation Pilot Plant (WIPP) has been measured to be  $\Phi = 4.07 \pm 0.14$  (sys)  $\pm 0.03$  (stat)  $\times 10^{-7} \text{cm}^{-2} \text{s}^{-1}$ , with a vertical intensity of  $I_v = 2.97_{-0.13}^{+0.14}$  (sys)  $\pm 0.02$  (stat)  $\times 10^{-7} \text{cm}^{-2} \text{s}^{-1} \text{sr}^{-1}$ . Simulations of muon-induced backgrounds identified several potential cosmogenic radionuclides, though only  $^{137}\text{Xe}$  is a significant background for the  $^{136}\text{Xe}$   $0\nu\beta\beta$  search with EXO-200. Muon-induced neutron backgrounds were measured using  $\gamma$ -rays from neutron capture on the detector materials. This provided a measurement of  $^{137}\text{Xe}$  yield, and a test of the accuracy of the neutron production and transport simulations. The independently measured rates of  $^{136}\text{Xe}$  neutron capture and of  $^{137}\text{Xe}$  decay agree within uncertainties. Geant4 and FLUKA simulations were performed to estimate neutron capture rates, and these estimates agreed to within  $\sim 40\%$  or better with measurements. The ability to identify  $^{136}\text{Xe}(n, \gamma)$  events will allow for rejection of  $^{137}\text{Xe}$  backgrounds in future  $0\nu\beta\beta$  analyses.

---

## Contents

<b>1</b>	<b>Introduction</b>	<b>1</b>
1.1	The EXO-200 detector	2
1.2	Cosmogenic backgrounds	3
<b>2</b>	<b>Muon flux</b>	<b>4</b>
2.1	Muon spectrum generation	4
2.2	Muon reconstruction and efficiency	5
2.3	Muon flux measurement	6
<b>3</b>	<b>Simulations of cosmogenic nuclide production</b>	<b>10</b>
3.1	MC generation	10
3.1.1	FLUKA	10
3.1.2	Geant4	11
3.2	Muon-induced activation	11
3.3	Prompt $\gamma$ s following neutron capture	12
<b>4</b>	<b>Veto-tagged data</b>	<b>14</b>
4.1	Data reconstruction and selection	14
4.2	Fit to data	16
4.3	Capture rates in data and simulation	17
<b>5</b>	<b>Conclusions</b>	<b>20</b>
<b>A</b>	<b>Expanded table of cosmogenic nuclides of interest</b>	<b>21</b>
<b>B</b>	<b>Veto-tagged data systematic effects</b>	<b>21</b>

---

## 1 Introduction

While neutrino oscillation experiments have demonstrated that neutrinos are massive particles, their behavior under CP conjugation (Dirac or Majorana) and the absolute value of their masses are still unknown. The observation of neutrinoless double-beta decay ( $0\nu\beta\beta$ ), a hypothetical lepton-number-violating decay mode, would demonstrate that neutrinos are Majorana particles and could determine the absolute neutrino mass scale. Certain even-even nuclei, such as  $^{136}\text{Xe}$  and  $^{76}\text{Ge}$ , are stable against ordinary  $\beta$  decay but have been observed to undergo two-neutrino double-beta decay ( $2\nu\beta\beta$ ) and are candidates for  $0\nu\beta\beta$  searches. Current limits on the half lives for the  $0\nu\beta\beta$  mode of  $^{136}\text{Xe}$  and  $^{76}\text{Ge}$  have reached the  $10^{25}$  year level [1–3]. Understanding and mitigation of all backgrounds is critical for further improvement.

Backgrounds to  $0\nu\beta\beta$  experiments can be divided into two main categories. First are those produced by long-lived radionuclides (typically U and Th). These can be mitigated through shielding, removal of surface activity, and careful materials selection during detector construction and design. Second are backgrounds induced by cosmic rays and their products. These cannot be completely shielded against, but certain techniques, as well as the use of

deep underground laboratories, can mitigate their impact on experimental sensitivity. This paper reports a study of cosmic-ray-induced backgrounds and, in particular, neutron capture, with EXO-200. Monte Carlo (MC) simulations and data taken with the detector were utilized for this purpose.

### 1.1 The EXO-200 detector

While a more complete description of the EXO-200 detector can be found elsewhere [4], the relevant features are discussed here. EXO-200 utilizes a time projection chamber (TPC) containing liquid xenon (LXe) enriched to 80.6%  $^{136}\text{Xe}$  ( $Q_{\beta\beta} = 2457.83 \pm 0.37$  keV [5]), with 19.1%  $^{134}\text{Xe}$ . The TPC has two drift regions, each with a signal readout, separated by a central cathode. The vessel is roughly 40 cm in diameter and 44 cm in length. Crossed wire planes at either end of the TPC provide induction and charge collection signals. Behind the wires, arrays of avalanche photodiodes (APDs) collect scintillation light. The collection and induction channels are known as the U-wires and V-wires, respectively. A teflon reflector surface is positioned just inside of the copper field rings. Signals from the wireplanes and APDs are digitized at 1 MS/s and saved in “frames” of  $\pm 1$  ms around a data trigger. The TPC is surrounded by a vacuum-insulated copper cryostat filled with HFE-7000 ( $\text{C}_3\text{F}_7\text{OCH}_3$  [6]) cryofluid, providing at least 50 cm shielding in any direction. The cryostat is surrounded by a lead shield of  $\sim 25$  cm thickness. The entire apparatus is located in a clean room  $\sim 655$  m underground at the Waste Isolation Pilot Plant (WIPP) near Carlsbad, NM. A rendering of the detector and shielding can be found in figure 1. This rendering includes a muon track passing through the TPC and all the muon secondary tracks.

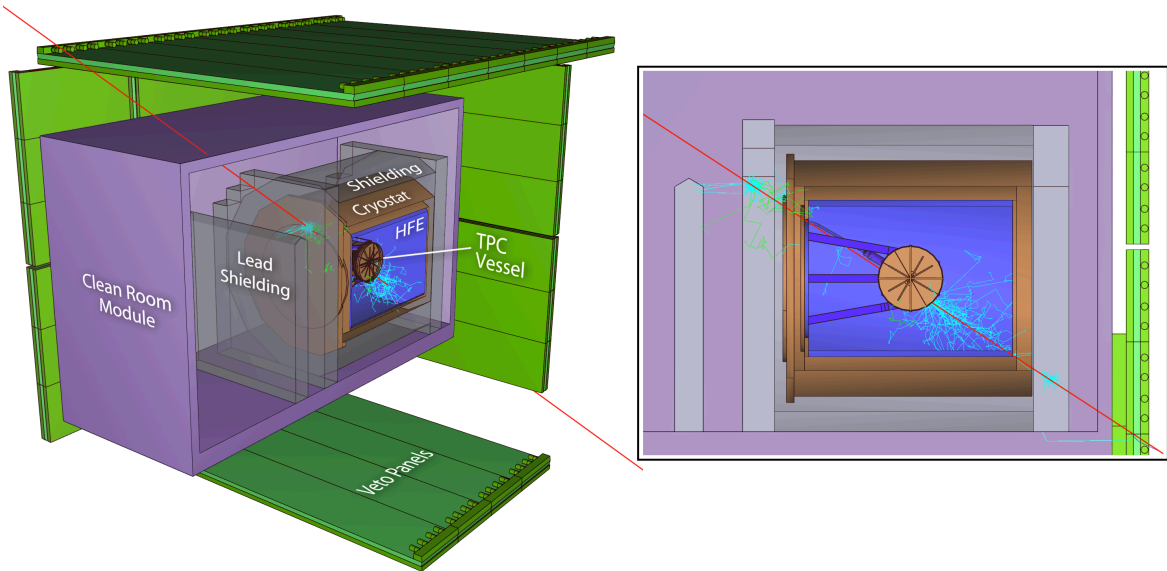


**Figure 1.** The EXO-200 cleanroom with various components labeled. The excavated cavern (not shown) extends  $\sim 60$  cm above the top veto panels and  $\sim 25$  cm below the bottom veto panels. The rendering was produced using our detector model with Geant4. A muon track (red) is included, along with photon (cyan) and neutron (green) tracks produced in the muon shower. An alternate view (in box on right) shows the shower more clearly.

EXO-200 has an active muon veto system. Scintillator panels, 5 cm-thick, are located on the outside of the cleanroom on 4 sides, providing  $96.35 \pm 0.11\%$  efficiency for tagging muons passing through the TPC. This allows tagging of prompt backgrounds associated with muons, such as neutron capture  $\gamma$ s and muon bremsstrahlung. The panels, refurbished from the concluded KARMEN experiment [7], also feature a 4 cm-thick polyethylene backing, loaded with 5% boron by mass. This provides structural support and some absorption of neutrons, though simulations indicate that the boron has little effect on cosmogenic neutron rates inside the cryostat.

The  $0\nu\beta\beta$  signals are distinguished from backgrounds through several active background suppression methods: scintillation-ionization ratio, energy, cluster multiplicity, and event position. The energy of interactions in EXO-200 is computed as a linear combination of collected charge and scintillation light. With an energy resolution of 1.53% at the  $0\nu\beta\beta$  Q-value [2], most radioactivity-induced backgrounds, including  $2\nu\beta\beta$ , can be actively suppressed using these analysis tools. Signals from  $\beta$  decays and  $\gamma$ -scattering are easily distinguished from  $\alpha$  decays in the xenon by the ratio of charge and scintillation light collected [8]. In  $0\nu\beta\beta$ , the sum kinetic energy of the emitted electrons equals the Q-value of the decay. While  $\beta$  decays tend to deposit their charge in a small volume of the detector,  $\gamma$ s of similar energy will Compton scatter and typically deposit energy in two or more positions (“clusters”). Charge clusters spatially separated by  $\sim 1$  cm or more can be resolved, allowing classification of events as single-site (SS), characteristic of  $2\nu\beta\beta$  and  $0\nu\beta\beta$ , or multi-site (MS), characteristic of  $\gamma$ -induced signals. Finally, the xenon, a high-Z material, is self-shielding to  $\gamma$  rays and is kept extremely pure. Nearly all  $\gamma$  backgrounds originate from outside the active xenon region [9]. The attenuation of external backgrounds in the LXe can be measured and fit to, providing further background identification [10]. The signal for  $0\nu\beta\beta$  is thus a set of SS events at the Q-value energy with the appropriate scintillation-ionization ratio which are uniformly distributed throughout the detector. The MS event set and SS events at other energies help characterize the composition of the remaining background.

## 1.2 Cosmogenic backgrounds

Cosmogenic muons may produce fast neutrons and unstable nuclides in underground detectors and shielding through several mechanisms, including muon spallation (virtual photon nuclear disintegration), muon elastic scattering on neutrons, photonuclear reactions from electromagnetic showers, nuclear capture of stopped muons, and secondary neutron reactions. These secondary neutron interactions, specifically neutron capture, are of particular interest to low-background studies with EXO-200.

Neutron capture may produce two signals in EXO-200. First, prompt  $\gamma$ s from nuclear de-excitation will be produced immediately after neutron capture. This prompt signal usually occurs in coincidence with triggers from the muon veto panels, and is thus rejected from the data set for the  $0\nu\beta\beta$  searches. Later, decay radiation from a generated radionuclide may produce delayed signals. The most prominent background contributor produced in the bulk of LXe is muon-induced  $^{137}\text{Xe}$   $\beta$  decay, with a half-life of 3.82 minutes [11]. Produced through  $^{136}\text{Xe}(n, \gamma)$ , this  $\beta$ -emitter (creating coincident  $\gamma$ s only  $33 \pm 3\%$  of the time [12]) typically passes the SS/MS rejection, and has a near uniform position distribution (similar to that of  $2\nu\beta\beta$  and  $0\nu\beta\beta$ ). The Q-value for this decay is  $4173 \pm 7$  keV [13], so the  $\beta$  spectrum overlaps the Q-value for  $0\nu\beta\beta$ . Indeed, in the most recent EXO-200  $0\nu\beta\beta$  search [2],  $^{137}\text{Xe}$   $\beta$  decay was fitted to contribute 7.0 counts to the SS region of interest ( $\pm 2 \sigma$  energy window), out of a total  $31.1 \pm 1.8(\text{stat.}) \pm 3.3(\text{sys.})$  counts, during a  $^{\text{enr}}\text{Xe}$  exposure of 123.7 kg  $\cdot$  yr.

Understanding and mitigating this background is important for improving  $^{136}\text{Xe}$   $0\nu\beta\beta$  analyses and for designing new experiments. Detection of the nuclear de-excitation that occurs after a neutron capture can be used to tag the production rates of this and other cosmogenic nuclides. We searched for neutron capture signals in EXO-200 TPC data coincident with muon veto panel triggers. This veto-tagged data allows us to search for and measure production of cosmogenic nuclides by neutron capture independently from the fit of low-background data (the dataset with vetoes applied, used for the  $0\nu\beta\beta$  analysis [2]).

Three separate but related studies are reported here. First, section 2 describes a measurement of the muon flux at WIPP, using data from muons passing through the EXO-200 TPC. The muon flux is needed to normalize simulations of cosmogenic backgrounds. Next, section 3 describes simulations of cosmic-ray muons and their products at EXO-200. Cosmogenic nuclide production rates are derived from these simulations and measured muon flux, providing a catalog of potential backgrounds to  $0\nu\beta\beta$ . Finally, section 4 describes the study of veto-tagged data to measure neutron capture rates on the EXO-200 detector and shielding materials. These measurements are used to validate the simulation results from section 3 and to demonstrate understanding of EXO-200 cosmogenic backgrounds.

## 2 Muon flux

### 2.1 Muon spectrum generation

The EXO-200 experiment can detect muons both using the veto scintillator panels and the TPC. While more muon events are available from the scintillator panels, the analysis is not statistically limited and studying muons passing through the TPC allows for lower systematic uncertainty and a better determination of the muon angular distribution. Owing to the crossed-wire nature of the charge measuring planes, only muons traveling at certain angles relative to the TPC are properly reconstructed with high efficiency. Hence, some knowledge of the underground muon angular distribution is required to determine the overall muon acceptance.

Simulations of cosmic-ray-induced muons were performed using the Geant4-based [14, 15] EXO-200 MC simulation software (“EXOsims”). A detailed description of this software, along with validation studies, can be found elsewhere [10]. The original simulation geometry was expanded with the addition of the muon veto panels and surrounding salt (the main component of the WIPP cavern walls). The muons were generated at a height of 3.5 m above the TPC center, from a horizontal circular plane 10.5 m in radius, in the salt above the experiment. This generation plane covers a solid angle of  $1.37\pi$  sr around the vertical direction, allowing 99.43% of the expected muon flux passing through the TPC to be simulated. The muons were generated with a charge ratio of  $N(\mu^+)/N(\mu^-) = 1.3$  [16]. We found our data was well described by a phenomenological muon angular distribution from Miyake [17]. This angular distribution is given by

$$I(h, \theta) = I(h, 0) (\cos \theta)^{1.53} e^{\alpha(\sec \theta - 1)h} \quad (2.1)$$

where  $h = 1050$  meters water equivalent (mwe), named “vertical depth” in the Miyake report, is treated as an empirical parameter rather than the physical depth,  $\theta$  is the angle with respect to vertical, and  $\alpha = -8.0 \times 10^{-4}$  (mwe) $^{-1}$ .

The muon energy spectrum was based on the energy distribution at the surface [16],

$$\frac{dN}{dE_0} \approx \frac{0.14E_0^{-2.7}}{\text{cm}^2 \text{ s sr GeV}} \left( \frac{1}{1 + \frac{1.1E_0 \cos \theta}{115 \text{ GeV}}} + \frac{0.054}{1 + \frac{1.1E_0 \cos \theta}{850 \text{ GeV}}} \right). \quad (2.2)$$

The underground energy  $E$  is related to the surface energy  $E_0$  at slant depth  $X$  (straight-line distance traveled by a muon for a particular angle) using:

$$E_0 = Ee^{bX} + \epsilon_\mu \left( e^{bX} - 1 \right) \quad (2.3)$$

with  $b = 3.5 \times 10^{-4}(\text{mwe})^{-1}$  [16] and  $\epsilon_\mu = 693 \text{ GeV}$  [18]. For our flat overburden site, we used a vertical depth of 1600 mwe to compute the slant depth, based on this measurement (see section 2.3) and others [19] of the total flux. The deviation between this value and the final depth reported in section 2.3 does not significantly affect the results of this analysis as the resulting difference in the muon energy distribution has a negligible impact on the detection efficiency. The apparent mismatch of the overburden and vertical depth parameter for the angular distribution will be discussed in section 2.3.

For the purpose of muon flux determination, a targeting method was used to avoid simulation of muons not directed near the TPC, so only 0.323% of muons passing through the generation plane were fully simulated. The targeting algorithm generated all muons which would, based on initial direction, pass through a cylinder of double the length and radius of the TPC.

## 2.2 Muon reconstruction and efficiency

In EXO-200, the muon track finding algorithm is substantially different from that used to reconstruct  $0\nu\beta\beta$  decays and radioactivity-induced events. A typical EXO-200 TPC muon event is shown in figure 2. Reconstruction requires an APD sum signal of at least 10000 ADC units, rejecting lower energy  $\beta$ s and  $\gamma$ s. Muon track signals are identified by searching the waveforms for an increase (decrease) of 80 counts beyond the baseline on the collection (induction) wires and finding the peak in time, here called a ‘‘hotspot’’. The collection of these hotspots in channel-time space is processed with a Hough transform [20] to identify the straight muon track and to derive the muon direction in space. At least 3 hotspots are required on U-wires and at least 3 on the V-wires. Additional cuts are applied to reject poorly fit muon tracks and noise events.

Reconstructed positions and directions are based on a right-handed Cartesian coordinate system, with origin at the TPC center, and with the  $z$ -axis along the TPC axis of symmetry and drift direction. Azimuthal and polar angles ( $\phi$  and  $\theta$ , respectively) are measured with respect to the vertical axis,  $y$ , with  $\theta = 0$  defined as straight down ( $-y$ ), and  $(\theta, \phi) = (\pi/2, 0)$  parallel to  $+z$ . The fit is applied to both halves of the TPC and, if both halves have a well-reconstructed track, the reconstructed direction from the TPC half with more hotspots on the track is selected. Comparing the directions of reconstructed tracks in events where the muon passes through both TPC halves has shown that this method works well. While small improvements may be possible through a combined fit of both TPC halves, we do not expect such a technique to improve statistical or systematic uncertainties in any significant way.

Vertical muons which pass parallel to the wireplanes do not typically have their direction reconstructed accurately, as there is no time difference between the arrival of charge on the different V- and U-wires. Poorly reconstructed muons often have their best fit direction nearly collinear with the U- or V-wires. To avoid these pathologies, we selected an angular region of interest (ROI) in which the muon track fitter gives accurate reconstructed angles, and we only used muons in that region for the flux measurement. Geant4-based MC studies were used to identify this well-behaved region, and their results are shown in figure 3.

Figure 4 shows measured muon track directions and the ratio of simulated to reconstructed angles from Monte Carlo simulation (MC). A total of 14810 muons were reconstructed

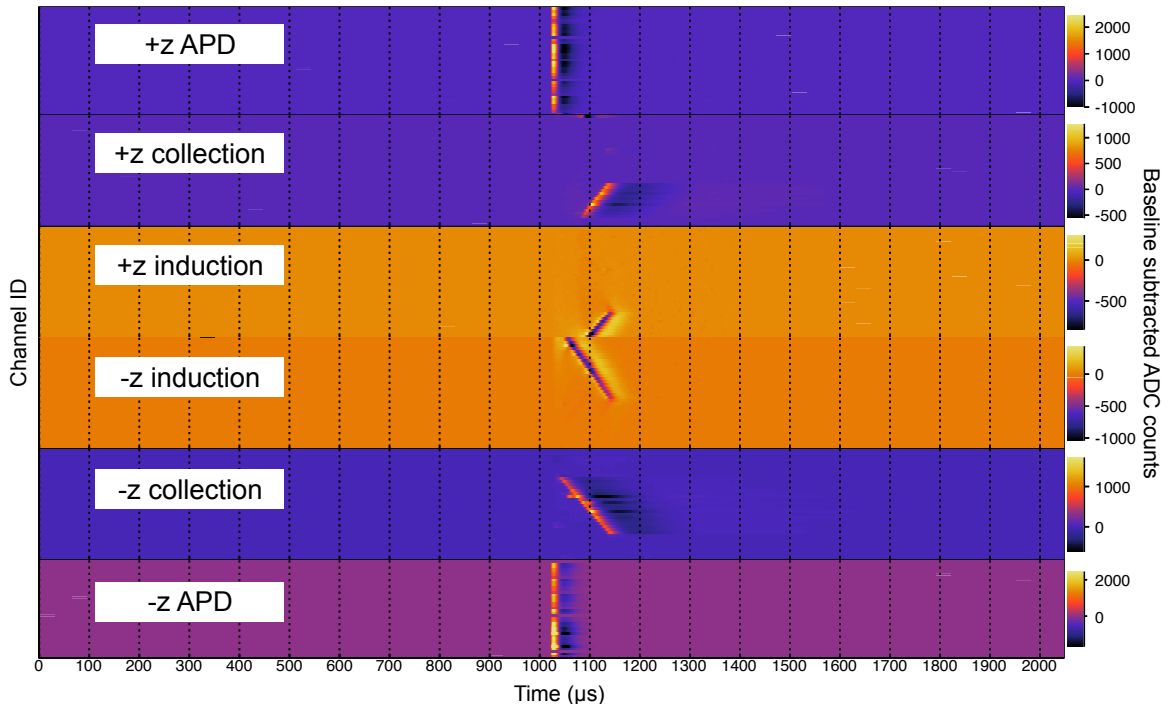


**Figure 2.** A typical muon track shown on U- and V-wires and APDs, taken from EXO-200 data. The color scale, indicating signal amplitude, is in baseline subtracted ADC units. There are 38 channels in each of the U- and V-wire planes, and 37 channels in each APD plane. The slope between the charge collection and induction channels and the time coordinate is used to reconstruct the direction of the muon. Because of the almost isotropic nature of light propagation inside the detector, the APD light pattern indicates only the time of scintillation and total light yield, and cannot help with direction reconstruction. In this particular event, the muon passes through the central cathode, so a charge signal is seen in both TPC halves.

in the angular ROI, representing 503.118 days livetime. The fraction of reconstructed muons with their reconstructed angle within the ROI (green-outlined region in the left panel of figure 4) is  $43.8 \pm 0.1\%$  ( $43.3 \pm 0.3\%$ ) in MC (data).

### 2.3 Muon flux measurement

The total flux is calculated as

$$\Phi = \frac{N_{\text{det}}}{\epsilon \Delta T A}, \quad (2.4)$$

with  $\epsilon$  the efficiency for a muon passing through the generation plane of area  $A$  to be detected within the angular ROI, and  $N_{\text{det}}$  the number of such muons detected in time  $\Delta T$ . MC studies showed that the fraction of muons passing through the generation plane (including muons not simulated because of targeting) which are reconstructed in the angular ROI is  $\epsilon = 2.46 \pm 0.05$  (stat)  $\times 10^{-4}$ , before systematic effects are accounted for.

A summary of our systematic uncertainty estimates and corrections is found in table 1. All systematic uncertainties are treated as independent, added in quadrature, and applied symmetrically to the result except for the uncertainty in angular distribution.



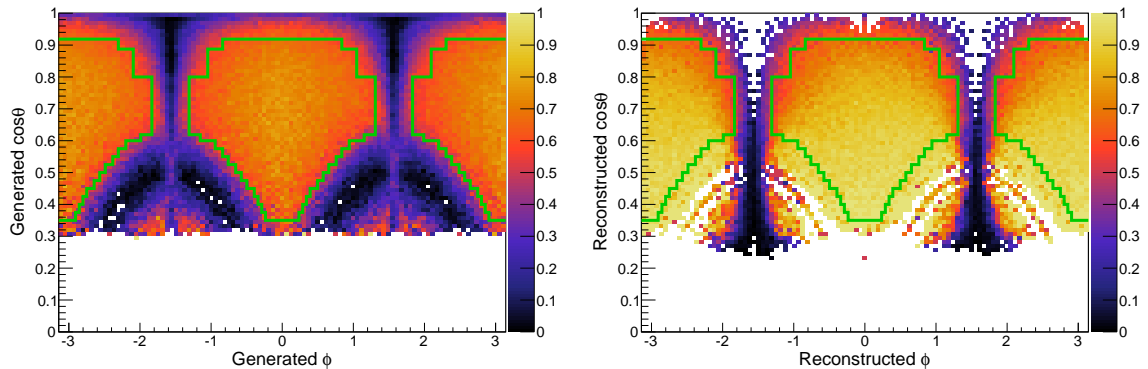


**Figure 3.** Monte Carlo determination of muon track reconstruction accuracy. The color scale indicates the probability for the angle to be reconstructed within  $5^\circ$  of the generated (true) angle. This is shown as a function of the generated (left) and reconstructed (right) azimuthal and polar angles ( $\phi$  and  $\theta$ , respectively) with respect to vertical. The angular region of interest (ROI), where reconstruction is deemed sufficiently accurate, is enclosed by green lines.

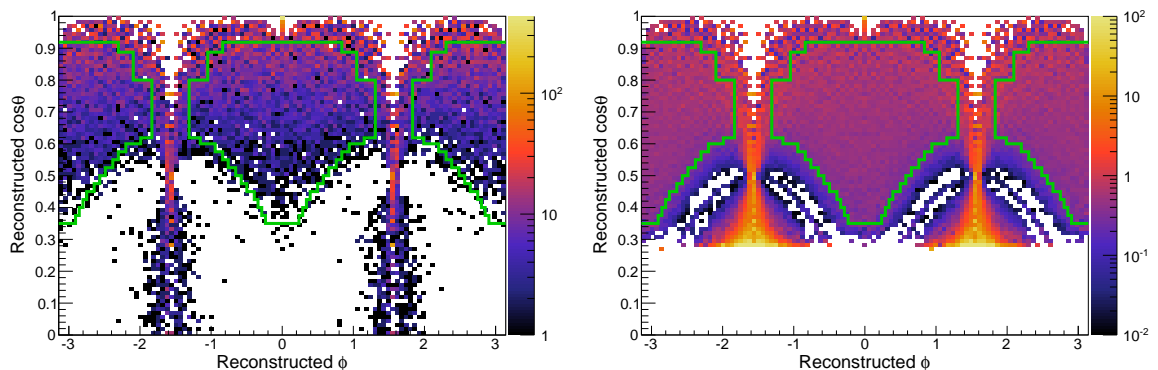


**Figure 4.** (left) The reconstructed muon directions from data. The color scale represents the absolute number of observed counts. (right) MC events, the color scale represents the ratio of reconstructed muons in each angular bin to muons simulated with that angle and directed at the active LXe. The angular region of interest (ROI) is enclosed by green lines. The excess of reconstructed muon angles near  $\phi = \pm\pi/2$  is due to the tendency for mis-reconstructed muons to be assigned angles parallel to the wireplanes.

The EXO-200 event reconstruction software identifies electronics noise-induced events with noise-finding algorithms. Unphysical signals such as large initial negative signals on the collection wires, simultaneous saturation of most channels, and unusual negative pulses in the APDs can trigger the noise finder [21]. Signals appearing to be muon tracks present in both TPC halves in a way which cannot be explained by a muon crossing the cathode are also tagged as noise. In rare cases, legitimate muon signals may be incorrectly tagged as noise, leading to a loss in detection efficiency. Our studies showed that the noise tagging rate differs slightly for muons in data and MC. A correction was obtained by examining data events rejected as electronics noise and identifying by visual inspection those which appear to be good muon events. The noise tag cut efficiency for good muons in data (MC) is 96.3%

Systematic	Correction value	Uncertainty value
TPC noise tagging efficiency	+3.0%	3.0%
Targeting efficiency	-0.51%	0.5%
Finite generation plane correction	-0.57%	—
Reconstruction efficiency	—	0.4%
ROI fraction	—	1.1%
MC statistical error	—	0.1%
Muon angular distribution	—	+3.2% ( $I_v$ ), +1.2% ( $\Phi$ ) -2.9%
Muon energy distribution	—	0.25%
Total systematic	+1.89%	+4.6% ( $I_v$ ), +3.5% ( $\Phi$ ) -4.4%

**Table 1.** Summary of systematic corrections and error estimates. All uncertainties are added in quadrature. Both corrections and uncertainties are listed here. The vertical intensity ( $I_v$ , see equation 2.6) and flux ( $\Phi$ ) calculations are affected by angular distribution uncertainties differently. The data statistical uncertainty is 0.8%.

(99.3%). The MC efficiency is corrected to match the data. Although corrected for, the 3% efficiency difference is taken as an uncertainty. We attribute this discrepancy to imperfect simulation of electronics behavior in MC.

Muons may scatter and therefore not travel on straight lines as assumed by our MC targeting. Performing a fit to the number of muons in the ROI as a function of closest distance of approach to active LXe, we estimated that a 0.51% correction to the targeting efficiency is necessary to account for contributions from scattered muons. Conservatively, we also treat this as an additional uncertainty.

The muon efficiency uncertainty was estimated using muons passing through the cathode (and thus producing a track in both TPC halves). The fraction of ROI muons in which the muon produces a valid track in the ROI in both TPC halves ( $f_{2\times\text{ROI}}$ ) is a function of the muon angular distribution and the reconstruction efficiency. As the angular distribution was already constrained by our data, we used the difference in  $f_{2\times\text{ROI}}$  values observed when comparing data and MC to estimate this uncertainty. The difference in the ratio of ROI muons vs. total reconstructed muons when comparing data and MC was used as an additional ROI rate uncertainty. This likely amounts to double-counting a single uncertainty, but we treated these as independent, adding them in quadrature, to be conservative.

Simulations were conducted to test whether any muon secondaries, created in showers, would reach the TPC and affect the reconstruction efficiency. No statistically significant effect was observed. A literature review [22, 23] showed that muon bundles are infrequent and diffuse enough to provide negligible impact to our measurement.

The choice of muon angular distribution was evaluated by comparing the measured  $\cos\theta$  distribution for events in our angular ROI to MC-produced events using several empirical angular distributions (Miyake [17], Mei [18], and Cassiday [24]). The phenomenological distributions were simulated for various values of the depth parameter  $h$ , at intervals of 50 mwe. We used a Pearson  $\chi^2$  statistic to quantify the difference between the measured and simulated angular distributions. The results are shown in figure 5.

The Miyake [17] distribution (equation 2.1) with  $h = 1050$  mwe gave the best agreement. Reconstructed  $\cos\theta$  and  $\phi$  distributions based on this optimal parameterization are shown overlaid with data in figure 6. The Cassiday [24] distribution gave slightly worse ( $\Delta\chi^2 = 3.4$ )

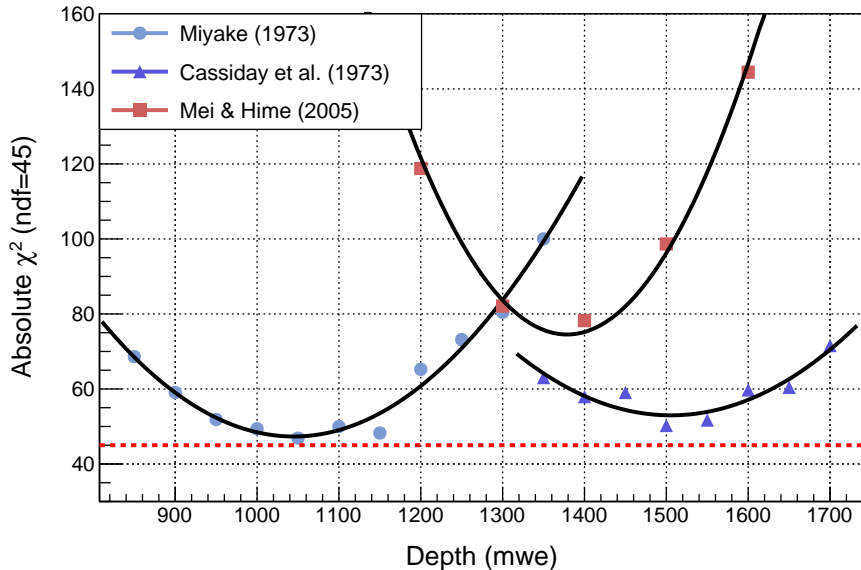


**Figure 5.** Pearson  $\chi^2$  between data and MC distributions of reconstructed  $\cos\theta$  for ROI muon events. The best-fit distribution was Miyake 1050 mwe, although Cassidy et al. provides a similar best  $\chi^2$  at 1500 mwe. Distributions from Miyake [17], Mei [18], and Cassidy [24] were considered. Parabolic fits were made to confirm the expected behavior and to better distinguish the true minima from artifacts due to statistical fluctuations.

agreement at a depth parameter of  $h = 1500$  mwe, which is closer to the physical depth of WIPP. As discussed before, we treat  $h$  as a free parameter of a phenomenological distribution, utilized to achieve good agreement between data and MC. Because we are directly measuring the angular distribution and not relying on a parameterization to be accurate, we can select the best-fitting distribution without concern for the intended physical meaning of  $h$ . We chose to absorb this choice into a systematic uncertainty due to angular distribution.

If there is an angular bias in reconstruction efficiency that is not present in MC, the angular distribution will be measured incorrectly. To account for this possibility, the same angular distribution variation was repeated after skewing the reconstruction efficiencies in such a way as to reflect the observed  $f_{2\times\text{ROI}} \cos\theta$  dependence. The resulting best-fit depths for Miyake and Cassidy were used to define a further systematic uncertainty to the angular distribution. The central value for flux was calculated assuming the Miyake 1050 mwe distribution with no efficiency skewing.

We also performed a test of the muon energy spectrum underlying the MC model by varying the  $\epsilon_\mu$  and  $b$  parameters in equation 2.3 in the ranges of 500 – 693 GeV and  $(3.0 - 4.0) \times 10^{-4} \text{ (mwe)}^{-1}$ , respectively. At the extremes, the simulations showed a 0.25% variation in measured flux, which was treated as an additional systematic uncertainty.

Adding all uncertainties in quadrature and applying the described corrections, the measured muon flux (flux crossing a flat horizontal surface from above) is

$$\Phi = 4.07 \pm 0.14 \text{ (sys)} \pm 0.03 \text{ (stat)} \times 10^{-7} \text{ cm}^{-2} \text{ s}^{-1}, \quad (2.5)$$

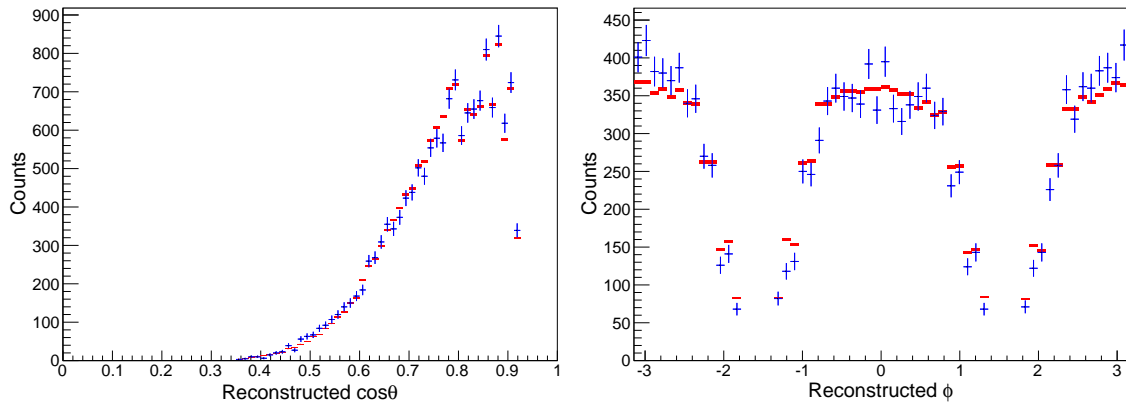


**Figure 6.** Distributions of  $\cos\theta$  (left) and  $\phi$  (right) for reconstructed muons in the angular ROI. Red rectangles are MC described by equation 2.1, blue crosses are data. The distributions are normalized to correspond to the same number of events in data and MC.

yielding a vertical muon intensity of

$$I_v = I_\mu(\theta = 0) = 2.97_{-0.13}^{+0.14} \text{ (sys)} \pm 0.02 \text{ (stat)} \times 10^{-7} \text{ cm}^{-2} \text{ s}^{-1} \text{ sr}^{-1}. \quad (2.6)$$

This corresponds to a standard depth of  $1624_{-21}^{+22}$  mwe by the evaluation of [25]. These results differ from those published earlier by Esch et al. [19]. The new flux measurement presented here is based on a measured angular distribution while the previous measurement assumed the Miyake distribution with a depth parameter now known not to reproduce the data well.

### 3 Simulations of cosmogenic nuclide production

#### 3.1 MC generation

Two MC simulation packages, FLUKA [26, 27] and Geant4 [14, 15], were used to model cosmogenic nuclide production. This approach allows us to evaluate the model dependence of neutron production and transport.

The EXO-200 analysis relies on simulations to model the detector response for neutron capture and all other processes measured. The estimation of capture  $\gamma$  detection efficiencies and calculation of probability density functions (PDFs) was performed with the same EXOSim software as for the muon flux estimation [10]. The model has been tuned for accurate low energy electromagnetic physics and incorporates particle interaction and electronic signals simulation. Different Geant4 physics models were used for simulating neutron production and transport, and for estimating cosmogenic nuclide production rates. In all muon-induced neutron production simulations, the best-fit muon angular distribution (Miyake 1050 mwe) was used, and the muon energy spectrum was based on the best-fit depth (1624 mwe).

##### 3.1.1 FLUKA

FLUKA version 2011.2c was used for the studies reported here. The simulation geometry is a simplified version of the geometry used in EXOSim, focused primarily on the general shapes, and geared towards the proper reproduction of objects of significant mass (see table 2). Thus,

features such as the cathode and TPC leg supports are neglected. The total mass of lead, cryostat, HFE-7000, xenon, and TPC copper are all simulated to better than 1% agreement with the Geant4 geometry and CAD reference designs.

The simulated geometry for the WIPP cavern includes 5 m of salt above EXO-200, 3 m on the floor and near walls, and 2 m thick walls at the ends of a  $\pm 9$  m long cavern. The salt was simulated as pure NaCl with 1% H<sub>2</sub>O by molecular fraction [28]. Studies of muon shower production in FLUKA with this material composition confirmed that 5 m overburden is sufficient for the muon shower to reach steady state for neutron production, and that neutrons rarely stray more than 3 m from the muon in a perpendicular direction. The muons were generated in a 15 m radius plane above the salt, requiring a correction of +4.9% to muon-induced activities to account for the flux expected to originate from beyond the finite generation plane, not simulated in this model.

The FLUKA simulation used the PRECISIO(n) defaults, with several other options activated for accurate treatment of cosmogenic secondaries. To achieve a detailed modeling of nuclear de-excitation we utilized EVAPORAT(ion) and COALESCE(nce). We activated photonuclear interactions and muon-muon pair production with PHOTONUC, heavy ion transport with IONTRANS, electromagnetic dissociation of heavy ions with EM-DISSO(ciation), and the PEANUT hadronic generator model at all energies with PEATHRES(hold). The rQMD-2.4 [29] and DPMJET-3.0 [30] models were activated. We additionally set electromagnetic transport cutoffs of 2 MeV and 600 keV for  $e^\pm$  and  $\gamma$ , respectively. All materials were associated with low energy neutron cross-sections assuming they have a temperature of 296 K. A study was performed comparing capture rates with 87 K cross-sections and 296 K cross-sections for materials within the cryostat, and a correction to approximate 167 K (the temperature of LXe) was derived by interpolating the neutron capture rates between these temperatures.

### 3.1.2 Geant4

For the neutron-related studies, Geant4 [14, 15] version 10.0.p02 was used. Photo-nuclear, electro-nuclear, muon-nuclear interactions and capture of muons on nuclei were enabled. The “QGSP\_BERT” model was used for hadronic interactions. A package of high-precision models for neutron interactions below 20 MeV was enabled and neutron data files with thermal cross sections of version 4.4 were used. An unreleased patch [31] was applied to correct photo-nuclear interaction rates.

Muons were generated with the same energy and angular distribution as was used with the FLUKA simulation. In this simulation, no generation plane was utilized. Rather, all muons passing through a sphere of 2 m radius, centered on the TPC, were simulated. The muons were generated from a spherical surface with 8 m radius, also centered on the TPC.

The masses for each of the major components in both simulations are listed in table 2.

## 3.2 Muon-induced activation

Many unstable nuclides are produced directly or indirectly by cosmogenic muons in the detector and shielding materials. Most of these nuclides are irrelevant because, given the attenuated muon flux underground, they are produced at very low rates. We considered unstable nuclides capable of producing events with energy near the  $0\nu\beta\beta$  Q-value. The rate of such events is effectively a product of muon flux, the probability to create specific nuclei per muon, and the efficiency of the subsequent decay to deposit energy in the  $0\nu\beta\beta$  energy ROI.

Material	Geant4 mass (kg)	FLUKA mass (kg)	Reference mass (kg)
TPC LXe	169.2	168.7	168.6
TPC vessel Cu	22.3	22.3	22.4
TPC internal Cu	10.2	10.3	10.4
HFE-7000	4138	4138	4140
Inner Cryo	2881	2841	2843
Outer Cryo	3480	3451	3453
Main Pb shielding	55060	54920	55000
Outer Pb wall	8620	8629	8634

**Table 2.** Major component masses from Geant4, FLUKA, and engineering-model reference values [4, 10]. Mass agreement between the Geant4, FLUKA, and CAD (reference) geometries is at the  $\pm 1\%$  level. TPC LXe includes all liquid xenon in the TPC vessel, including xenon outside the teflon reflector or behind the collection wires. Xenon in the TPC support legs or elsewhere in the circulation loop is not included in the mass accounting. TPC internal Cu includes all copper parts within the TPC vessel.

A list of nuclides of interest is shown in table 3. Most of these nuclides are produced in xenon, as  $\beta$  decays in xenon are especially important sources of background for  $0\nu\beta\beta$  searches.  $^{135}\text{Xe}$  is included in this table due to its high production rate, although it cannot mimic  $^{136}\text{Xe}$   $0\nu\beta\beta$ .  $^{60}\text{Co}$  contributes to  $0\nu\beta\beta$  background via coincidence summation of its two principal  $\gamma$ s. Therefore,  $^{60}\text{Co}$  is only a problem in detector components in and near the TPC. The underground, steady-state production of  $^{60}\text{Co}$  in copper provides a negligible contribution compared to the left-over activity from above-ground exposure [9]. The total number of atoms of each unstable nuclide generated per unit time is noted, along with two efficiencies. We have evaluated the efficiency to deposit between 2.3 and 2.6 MeV in the xenon fiducial volume (FV) and, in addition, the efficiency for an event to pass the EXO-200  $0\nu\beta\beta$  selection cuts, which require SS event topology and an energy deposition in the  $Q_{\beta\beta} \pm 2\sigma$  energy window (the  $0\nu\beta\beta$  ROI) [2]. All cosmogenic radionuclides other than  $^{137}\text{Xe}$  make a negligible contribution to the SS  $0\nu\beta\beta$  ROI backgrounds. Each is calculated to contribute less than 1% of the contribution from  $^{137}\text{Xe}$ . An expanded table of nuclides of interest is found in appendix A.

All daughters of the initial radionuclides are either stable or have no ability to contribute near the  $0\nu\beta\beta$  Q-value. We also considered known metastable states for nuclides produced in xenon, and found that none of them contribute significantly to backgrounds.

The background contribution from iodine isotopes is almost certainly over-estimated, because iodine atoms are removed by the continuous xenon purification. It is difficult to calculate the xenon circulation patterns, so this effect is not considered here. Cosmogenic nuclides produced in the liquid xenon outside the TPC were also studied. A higher rate of activation was found nearer to the outside of the cryostat, but its contribution to  $0\nu\beta\beta$  backgrounds was found to be negligible, due to the low mass of xenon outside the TPC and a flow rate which allows most  $^{137}\text{Xe}$  to decay before reaching the TPC.

### 3.3 Prompt $\gamma$ s following neutron capture

Veto-tagged data studies (section 4) require accurate modeling of signals due to prompt  $\gamma$ s from neutron captures on detector materials. While FLUKA and Geant4 include models for

Region/ Nuclide	Half- life	Total energy (keV)	2.3–2.6 MeV efficiency	EXO-200 SS ROI efficiency	Geant4 rate (yr <sup>-1</sup> )	FLUKA rate (yr <sup>-1</sup> )
HFE-7000 <sup>16</sup> N	7.1 s	10420	0.015%	0.001%	2380 ± 90	2910 ± 110
TPC vessel <sup>60</sup> Co	5.3 y	2823	0.19%	0.0002%	2.6 ± 0.3	2.9 ± 0.6
TPC LXe <sup>130</sup> I	12 h	2949	8.5%	0.001%	7.3 ± 0.5	21.6 ± 1.8
TPC LXe <sup>132</sup> I	2.3 h	3581	5.5%	0.013%	7.7 ± 0.5	22.2 ± 1.8
TPC LXe <sup>134</sup> I	53 m	4175	4.5%	0.012%	7.3 ± 0.5	20.4 ± 1.7
TPC LXe <sup>135</sup> I	6.6 h	2627	2.9%	0.035%	8.6 ± 0.6	21.6 ± 1.8
TPC LXe <sup>135</sup> Xe	9.1 h	1165	—	—	1110 ± 40	1060 ± 40
TPC LXe <sup>137</sup> Xe	3.8 m	4173	4.1%	1.5%	439 ± 17	403 ± 16

**Table 3.** Summary of cosmogenic radionuclides of interest. All listed nuclides decay through  $\beta$ -emission, some with associated  $\gamma$ s. The half-lives and total decay energy are listed [13, 32–37]. The efficiencies listed have been estimated using EXOSim. The Geant4 and FLUKA columns give the estimated production rate for the listed nuclide in atoms per year. Iodine efficiencies listed do not account for iodine removal during recirculation. Only the <sup>137</sup>Xe production is dominated by thermal neutron capture, so the FLUKA temperature correction has been applied only to that nuclide. Uncertainties include the MC statistical uncertainty and the muon flux uncertainty. Significant differences in the predicted rates from FLUKA and Geant4 were seen for nuclides (such as the iodine isotopes) which are primarily produced with high energy ( $E > 10$  MeV) interactions.

simulating prompt  $\gamma$ s after neutron capture, better accuracy can be achieved using custom capture  $\gamma$  cascades. These cascades were used in EXOSim to generate PDFs for fits to data. In each case, the  $\gamma$ s in the cascade are distributed isotropically, and, with the exception of HFE-7000, captures were generated uniformly in each volume. Our simulations showed that thermal neutron capture is the dominant event class in the data, so the cascades were all based on thermal capture measurements.

- <sup>137</sup>Xe atoms are produced in a capture state with excited state energy  $4025.46 \pm 0.27$  keV [38]. They relax into the ground state promptly, primarily through  $\gamma$  emission. The main <sup>136</sup>Xe( $n, \gamma$ )<sup>137</sup>Xe cascade was modeled using thermal neutron capture data by Prussin et al. [39]. The evaluated  $\gamma$  and level data were converted into a de-excitation chain model to generate the cascade. For levels where an imbalance exists between incoming and outgoing  $\gamma$  intensity, it was assumed that an unknown “continuum” state exists, and the imbalance was resolved with an additional transition to a randomly chosen level in the continuum. To evaluate possible systematic uncertainties in this important capture cascade, a simulation was conducted based on preliminary data from a measurement of <sup>136</sup>Xe( $n, \gamma$ )<sup>137</sup>Xe at the Detector for Advanced Neutron Capture Experiments. The DICEBOX code [40] was used to help model the cascade. Efficiency differences between this model and the primary model are treated as a systematic uncertainty.
- <sup>1</sup>H( $n, \gamma$ )<sup>2</sup>H results in the emission of a single  $\gamma$  with an energy of 2223 keV. As the HFE-7000 volume is much thicker than the thermal neutron interaction length, we divided its volume into 6 concentric cylindrical shells of roughly equal thickness for simulation in EXOSim and FLUKA, to account for the varying capture rates and spectral variations at different positions.

- The capture cascades for  $^{63,65}\text{Cu}(n, \gamma)^{64,66}\text{Cu}$  were based on levels and  $\gamma$ s extracted from the ENSDF database [41, 42]. Level transitions were matched by automated parsing of the data file [43], producing code for modeling the cascade.
- The capture cascade for  $^{19}\text{F}(n, \gamma)^{20}\text{F}$  was similarly based on levels and  $\gamma$ s extracted from the ENSDF database [44].
- We found no publications specifically measuring the branching ratios of the capture cascade for  $^{134}\text{Xe}(n, \gamma)^{135}\text{Xe}$ , so we used the cascade model included in FLUKA. This cascade is based on a study of neutron capture in natural xenon [45]. Including this PDF improves the overall fit to veto-tagged data, yet has only a small effect on the final fitted rate of capture on  $^1\text{H}$  and  $^{136}\text{Xe}$ , so cascade model uncertainties do not significantly affect the results.

Our simulations showed that only captures on  $^{134,136}\text{Xe}$  (in the TPC),  $^{63,65}\text{Cu}$  (in the TPC vessel, inner and outer cryostats), and  $^{19}\text{F}$  and  $^1\text{H}$  (in the HFE-7000) contribute significantly to veto-tagged neutron capture signals in EXO-200. Other possible captures, such as on carbon in the HFE-7000 or on the lead shield, were neglected, due to a combination of low cross-sections, low masses, and/or low  $\gamma$  detection efficiency in the TPC.

## 4 Veto-tagged data

By selecting events collected shortly after any of the 29 muon veto panels trigger, we obtained a “neutron-enriched” dataset. While not all veto panel triggers are associated with neutron events, the narrow time cut rejects the vast majority of non-cosmogenic events, leaving little other than neutron capture signals.

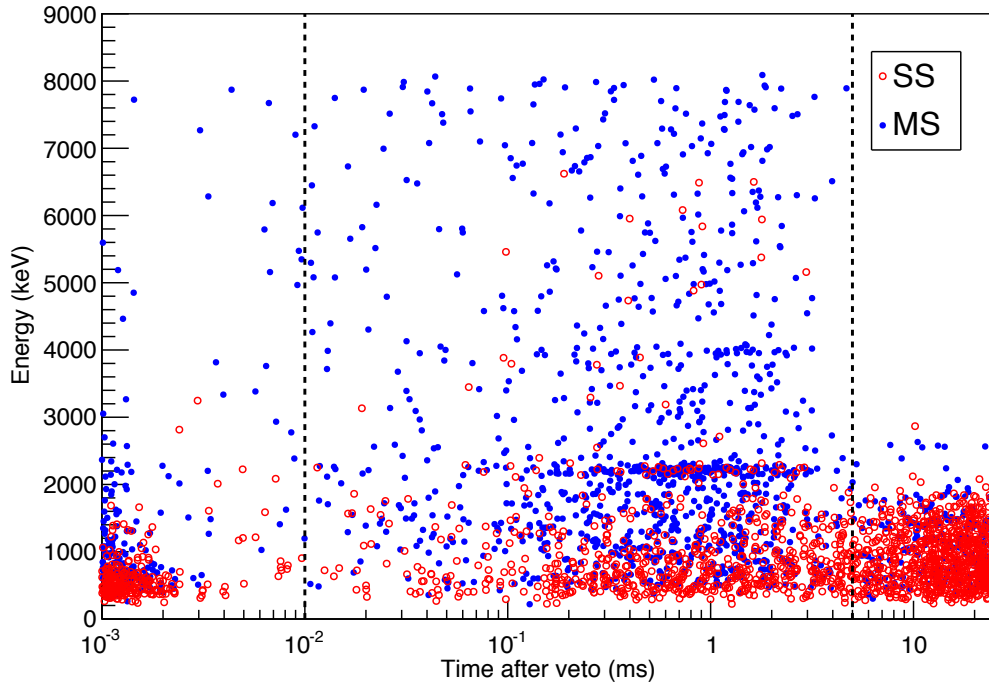
Figure 7 shows the data in and around the veto cut. We selected TPC events following a veto-panel trigger by times between 10  $\mu\text{s}$  and 5 ms. This lower bound rejects signals associated directly with the muons (such as bremsstrahlung  $\gamma$ s) while keeping the vast majority of neutron capture events. There are very few random coincidences with non-cosmogenic radioactive decay. This time window was chosen based on studies of signals from neutron capture on  $^1\text{H}$ , which produces a 2223 keV  $\gamma$ . Other prominent capture signals in the tagged data include  $^{136}\text{Xe}(n, \gamma)^{137}\text{Xe}$  (sum peak line at 4025 keV) and  $^{63,65}\text{Cu}(n, \gamma)^{64,66}\text{Cu}$  ( $\gamma$  spectrum up to 7916 keV).

### 4.1 Data reconstruction and selection

This analysis used the data set and analysis techniques of the recent  $0\nu\beta\beta$  analysis [2], but with modified event reconstruction and selection. Briefly, the  $0\nu\beta\beta$  analysis uses energy depositions in the TPC fiducial volume from isolated  $\gamma$  and  $\beta$  emissions to identify backgrounds and possible signals. Changes were focused on improving the efficiency for detecting capture  $\gamma$ s (as opposed to selecting the  $0\nu\beta\beta$  signal). Reconstruction changes include:

- The signal-finding and clustering algorithms were modified to better identify signals sharing frames with other signals, either from capture  $\gamma$ s or TPC muons.
- Denoising [2] of APD signals was not used. The denoising algorithm was developed for sparse events and does not cope well with short times between scintillation events. Choosing to forgo the denoising results in higher acceptance at the cost of slightly degraded energy resolution.

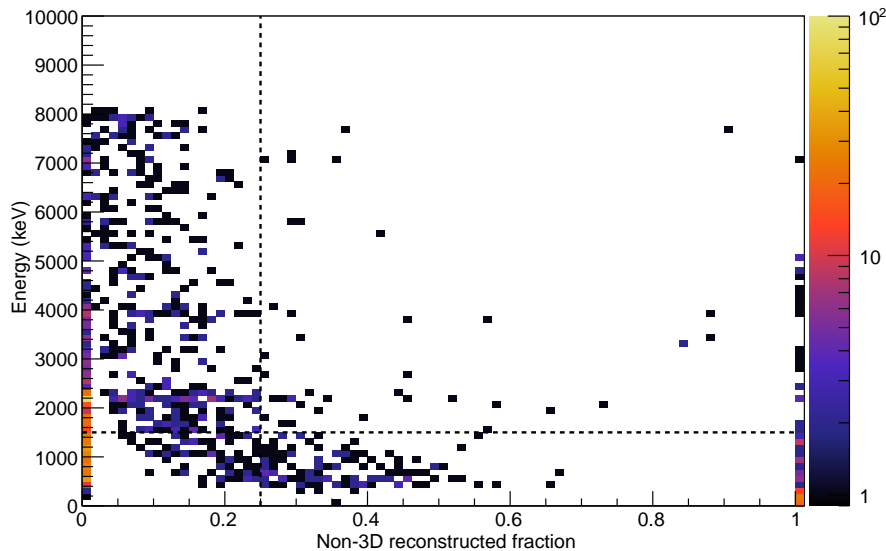




**Figure 7.** Data events occurring shortly after muon veto panel triggers. The event selection criteria are defined in Section 4.1. Filled (open) points represent MS (SS) events. The time axis is logarithmic. Signals from capture on  $^1\text{H}$  (population at 2223 keV),  $^{136}\text{Xe}$  (population at 4025 keV), and  $^{63,65}\text{Cu}$  (spectrum cutting off at 7916 keV) are visible in the data. The dashed vertical lines indicate the selection used to obtain the veto-tagged data set. At very short time differences, signals from muon-related processes other than thermal neutron capture dominate. At long time differences, radioactivity-induced events (largely SS  $2\nu\beta\beta$  events) dominate.

Event selection changes include:

- The fiducial volume was expanded slightly toward the cathode, requiring  $182 \text{ mm} > |z| > 5 \text{ mm}$  with a hexagonal cut in  $x-y$  with a 162 mm apothem.
- Events containing clusters without a full 3D position were accepted. In cases where a signal on a U-wire cannot be matched with that of a V-wire, the  $x-y$  position of the charge cluster cannot be determined. Rather than reject such events, we required that at least 75% of the total charge cluster energy be found in fully 3D reconstructed clusters. This greatly boosts efficiency for events with multiple Compton scatters. Figure 8 shows the fully 3D reconstructed fraction for MS events. The FV cut was only enforced along the  $z$ -direction (drift direction) for charge clusters without a determined  $x-y$  position.
- Events with more than one scintillation cluster ( $N_{\text{scint}} > 1$ ) in the data frame were accepted. Scintillation clusters within  $119 \mu\text{s}$  (a drift time plus uncertainty) of other scintillation clusters were rejected, as the charge drift times may overlap.
- No veto rejection was applied for events close in time to TPC muons, muon veto panel triggers, or other TPC events.



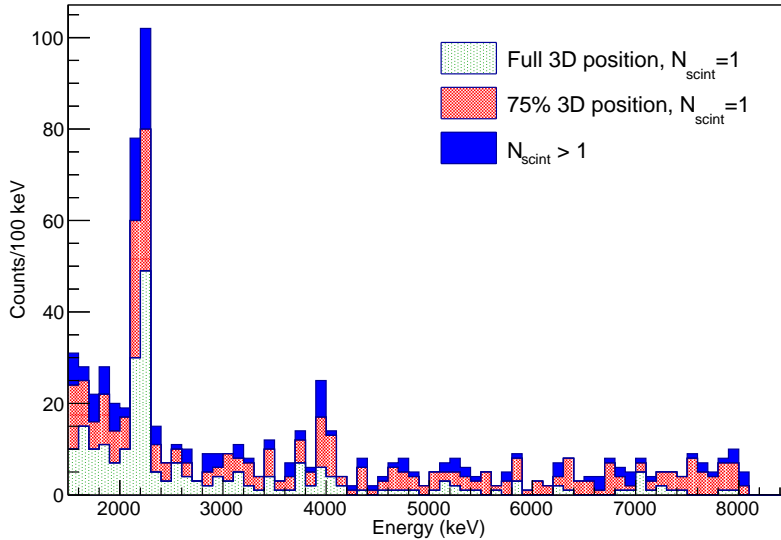
**Figure 8.** Event energy vs. non-3D reconstructed fraction for veto-tagged data. The color scale indicates the number of MS events in a bin. Events to the right of the vertical dashed line or below the horizontal one were rejected. The far left bins are fully-3D reconstructed events, and the far right bins have no charge clusters with a 3D position.

Figure 9 shows how the MS dataset grew with the addition of multi-scintillation cluster events and the relaxing of the 3D reconstruction cut. These modifications more than doubled the efficiency for neutron capture events, relative to the  $0\nu\beta\beta$  event selection criteria.

## 4.2 Fit to data

To measure the rate of neutron capture on each of the detector components, we performed a maximum-likelihood fit simultaneously in the SS and MS event energy and in the standoff distance parameter (nearest distance between a charge cluster and the teflon reflector or anode plane). The analysis threshold was 1500 keV, chosen to minimize complications related to partially 3D reconstructed events. We fitted with six fully independent PDFs: capture on  $^{136}\text{Xe}$ ,  $^{134}\text{Xe}$ ,  $^1\text{H}$ ,  $^{19}\text{F}$ , and  $^{63,65}\text{Cu}$ , plus one more PDF accounting for radioactivity-induced background events. The components of this background PDF were constrained to have relative contributions as measured using a fit of non-veto-tagged data. The HFE-7000 capture PDFs were composed of component PDFs representing six concentric geometric shells (see section 3.3). The copper capture PDF was also composed of six component PDFs, describing neutron capture on  $^{63}\text{Cu}$  and  $^{65}\text{Cu}$  in TPC vessel, inner cryostat, and outer cryostat. The fractional contribution of each of the HFE-7000 shells or copper components to their sum PDFs were determined by MC predictions, and were constrained with a 20% gaussian uncertainty during fitting. The constraint was used as these component PDFs are degenerate with each other in energy and standoff parameter, so the fitting process itself has little power in resolving, for example, the relative capture rates on the TPC vessel and cryostat.

We fitted using the same techniques used in previous analyses [2, 10], including a SS fraction constraint (constraining the event number ratio (SS/SS+MS) for each PDF), and



**Figure 9.** Histogram showing the effect of relaxing the 3D reconstruction cut and the  $N_{\text{scint}} = 1$  cut on MS veto-tagged data.

an overall normalization constraint (constraining detector efficiency). These are gaussian constraints with widths of 5.3% and 10.5% respectively, and represent uncertainties derived from source data studies. The  $\beta$ -scale (summarized by the parameter  $B$ , the correction needed to convert calibrated  $\gamma$  energies into  $\beta$  energies,  $E_\beta = BE_\gamma$  [2]) was determined with a fit to the non-veto-tagged data, yielding  $B = 0.998 \pm 0.004$ . This parameter was fixed to the central value, though it had little effect as the veto-tagged data is dominated by capture  $\gamma$ s.

The MS energy spectrum and PDFs fitted to the data are shown in figure 10. To obtain a final number of counts with uncertainties, profile-likelihood scans were performed over the number of counts in each of these PDFs. Examples are shown in figure 11.

The validity of our fit model was demonstrated by the small deviations of the SS event fractions and degenerate PDF fractions from the values determined from simulation. The SS fractions for the PDFs varied by between  $-0.15\%$  and  $-0.49\%$  from their central values, small changes relative to the 5.3% constraint. The degenerate PDF ratios (20% constraint) typically varied by  $\sim 1\%$ , with the maximum deviations  $-4.64\%$  for the  $^{63}\text{Cu}$  TPC vessel and  $+4.24\%$  for the innermost shell of HFE-7000  $^1\text{H}$ . If there were problems with the capture model, such as significant unaccounted-for PDFs, larger deviations would be expected.

The various efficiencies and uncertainties for capture on  $^{136}\text{Xe}$  and  $^1\text{H}$  are listed in table 4. Several of these efficiencies are highly affected by pile-up and detector inefficiencies related to muon-induced events. As these efficiencies are unique to this veto-tagged data analysis, details for their evaluation are presented in appendix B.

### 4.3 Capture rates in data and simulation

The best-fit results for the number of counts above 1500 keV in each of the PDFs are shown in table 5, along with the extrapolation to total number of captures. The expected numbers of captures from the FLUKA and Geant4 simulations are also included.

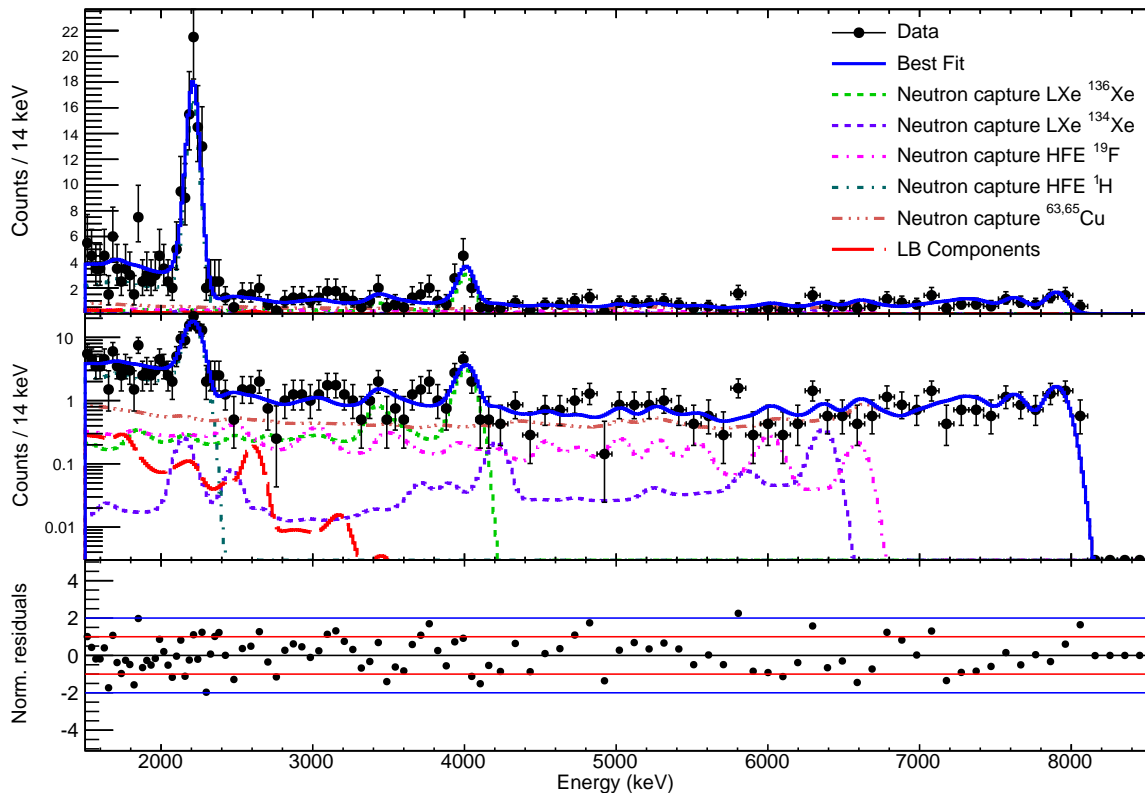


**Figure 10.** MS spectrum and the veto-tagged data fit. The SS spectrum and standoff distances were fit simultaneously with this. The different panels show results on a linear scale, logarithmic scale, and residuals, from top to bottom. The energy-binned fit is performed with 14 keV bins, though the binning shown here is modified and non-uniform to preserve spectral details while avoiding sparsely populated bins.

This comparison between captures determined with our models alone (without data input) and measured captures allows us to evaluate the simulations. Based on the rate of capture on  $^1\text{H}$  (with the smallest measurement uncertainty), FLUKA and Geant4 are over-estimating neutron capture by  $45^{+33}_{-25}\%$  and  $3^{+23}_{-18}\%$ , respectively. Using capture on  $^{136}\text{Xe}$  to evaluate this, the over-estimates go to  $19^{+45}_{-34}\%$  and  $30^{+49}_{-37}\%$ , respectively. It is not clear whether this is due to differences in simulated neutron production rates or capture cross-sections. This level of discrepancy ( $\sim 40\%$ ) is common for neutron production/transport simulations [48–51].

As the EXO-200 detector is a complex system with large masses of copper, enriched xenon, lead, and HFE-7000, it is difficult to identify any particular process which is not being simulated exactly. Despite the discrepancies and significant measurement uncertainties, this is a useful validation for both simulation packages, demonstrating reasonable performance with relevant neutron production and capture targets, such as enriched xenon.

The  $0\nu\beta\beta$  low-background fit (based on the  $0\nu\beta\beta$  analysis [2]) measures a  $^{137}\text{Xe}$  decay rate of  $374^{+135}_{-93}$  decays per year. As seen in table 5, this is consistent, within uncertainties, with the measured production rate from capture  $\gamma$ s ( $338^{+132}_{-93}$ ), and with the production rates

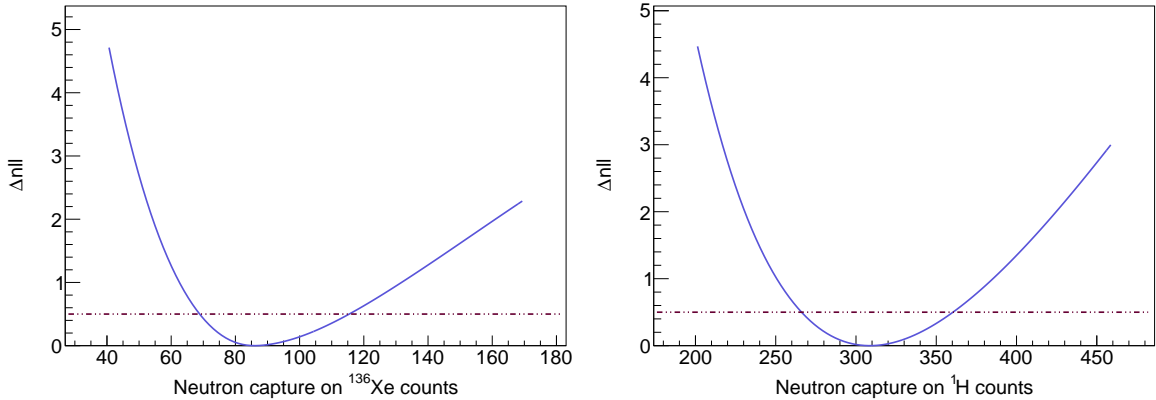


**Figure 11.** Profile likelihood for various values of fitted capture counts on  $^{136}\text{Xe}$  (left) and  $^1\text{H}$  (right). The vertical axis is the difference in the fit negative log likelihood (nll) between a particular number of counts and the best-fit value. A dashed horizontal line represents the  $1\sigma$  confidence level, assuming the validity of Wilks’ theorem [46, 47]. The resulting fits yielded  $86.0^{+29.4}_{-17.2}$  for  $^{136}\text{Xe}$  and  $309^{+52}_{-43}$  for  $^1\text{H}$  at  $1\sigma$ .

Systematic	$^1\text{H}$ efficiency	$^1\text{H}$ uncertainty	$^{136}\text{Xe}$ efficiency	$^{136}\text{Xe}$ uncertainty
Normalization constraint	–	10.5%	–	10.5%
— Noise tagging	–	0.4%	–	0.4%
— 3D reconstruction	–	4.3%	–	4.3%
— Overall efficiency	–	9.6%	–	9.6%
Capture cascade	–	–	–	0.9%
Multi- $\gamma$ efficiency	–	–	–	8.4%
Capture position distribution	–	7.7%	–	1.8%
Veto panel trigger	95.7%	1.7%	96.0%	1.7%
Veto time window	98.7%	2.5%	98.2%	4.8%
Muon-capture pile-up	94.7%	4.8%	88.8%	11.2%
Drift time cut	85.2%	7.1%	76.7%	11.7%
Frame-edge effects	97.1%	1.6%	97.1%	1.6%
Total systematic efficiency	74.2%	12.3%	62.4%	19.1%
Single capture efficiency	0.126%	–	29.6%	–

**Table 4.** Summary of veto-tagged data efficiencies and systematic uncertainties. All uncertainties are added in quadrature to arrive at the total uncertainty. The combination of efficiencies for different shells of HFE-7000 is complicated by the varying number of captures on each shell, so the total efficiency and uncertainty for  $^1\text{H}$  are not simply related to the individually evaluated efficiencies and uncertainties. Noise tagging, 3D reconstruction and overall efficiency are all included in the normalization constraint in the fit; all other terms are applied after fitting. The systematic efficiency is due entirely to effects associated with the veto-tagged nature of the data and proximity to other signals. Single capture efficiency is the efficiency for an isolated veto-tagged capture to produce a signal passing the analysis cuts, in the absence of these systematic effects.

computed from the FLUKA and Geant4 simulations (403 and 439, respectively). The capture detection efficiencies for nuclides other than  $^{136}\text{Xe}$  and  $^1\text{H}$  have larger, difficult to evaluate un-

PDF	Best-fit counts	Measured captures/year	Geant4 captures/year	FLUKA captures/year
Low-background	$35.9 \pm 11.7$	–	–	–
Copper capture	$306^{+70}_{-54}$	$4.23^{+1.30}_{-1.15} \times 10^5$	$4.69 \times 10^5$	$5.78 \times 10^5$
$^{19}\text{F}$ capture	$87.1^{+38.0}_{-35.1}$	$2.85^{+1.29}_{-1.20} \times 10^4$	$2.75 \times 10^4$	$2.45 \times 10^4$
$^1\text{H}$ capture	$309^{+52}_{-43}$	$2.41^{+0.50}_{-0.44} \times 10^5$	$2.48 \times 10^5$	$3.50 \times 10^5$
$^{134}\text{Xe}$ capture	$20.1^{+18.2}_{-13.9}$	$72.9^{+67.1}_{-52.0}$	116	120
$^{136}\text{Xe}$ capture	$86.0^{+29.4}_{-17.2}$	$338^{+132}_{-93}$	439	403

**Table 5.** Summary of the results of the veto-tagged fit and simulations. The best-fit counts are the total (SS and MS) number of counts above 1500 keV. This is based on a simultaneous fit in energy and standoff distance for SS and MS, while profiling over the number of capture counts. Final capture rates are for all captures. Component masses can be found in table 2. Only captures on  $^1\text{H}$  and  $^{136}\text{Xe}$  are considered to have fully validated systematics, as other capture PDFs have high uncertainties for capture cascade and/or capture timing efficiency. Measured capture rates are provided for these more uncertain PDFs for completeness. Uncertainties on simulation predictions are not listed, but are dominated by the 3.5% uncertainty on measured muon flux.

certainties due to much higher resonant neutron capture rates, capture cascade uncertainties, and/or lower statistics, so careful comparison to simulation is not attempted.

A search of low-background data showed no evidence for significant  $^{136}\text{Xe}$  neutron capture out of coincidence with the muon veto. At the  $1 \sigma$  C.L., no more than 10% of the  $^{137}\text{Xe}$  production is due to non-cosmogenic sources, and the best-fit rate is nearly zero. This is consistent with simulations (using SOURCES4A [52], FLUKA, and Geant4) of expected  $(\alpha, n)$  and spontaneous fission neutrons coming from the salt surrounding the detector cavern. It is notable that the copper cryostat and TPC, along with the HFE-7000 bath, manage to very effectively shield the xenon from radioactive sources of thermal neutrons, leaving only cosmogenic neutrons to produce significant backgrounds.

Identification of neutron captures can be used to remove  $^{137}\text{Xe}$  decays from the  $0\nu\beta\beta$  analysis data set. Such a veto would last several half-lives, and could be targeted to only reject signals in parts of the TPC where the capture was observed. This veto will be optimized and implemented in future  $0\nu\beta\beta$  analyses using  $^{136}\text{Xe}$ .

## 5 Conclusions

We have used the EXO-200 TPC to perform a measurement of the muon flux at WIPP, finding a vertical intensity of  $I_v = 2.97^{+0.14}_{-0.13} (\text{sys}) \pm 0.02 (\text{stat}) \times 10^{-7} \text{cm}^{-2} \text{s}^{-1} \text{sr}^{-1}$ , and a flux of  $\Phi = 4.07 \pm 0.14 (\text{sys}) \pm 0.03 (\text{stat}) \times 10^{-7} \text{cm}^{-2} \text{s}^{-1}$ . We used this measurement to normalize MC model calculations for cosmogenic neutron production, transport and capture, and cosmogenic radionuclide production. The only cosmogenic radionuclide found to have a significant contribution to  $0\nu\beta\beta$  backgrounds is  $^{137}\text{Xe}$ . Other possible cosmogenic backgrounds include several radioisotopes of iodine, but these were found to contribute much less than 0.1 counts per year to the EXO-200 ROI for  $0\nu\beta\beta$ , based on MC simulations.

We also directly measured cosmogenic neutron capture by looking at the capture cascades in data coincident with veto triggers. This technique yielded an estimate of  $338^{+132}_{-93}$  captures on  $^{136}\text{Xe}$  per year. This is in agreement with the observed  $^{137}\text{Xe}$  decay rate and

the estimates from FLUKA and Geant4. In general, both simulations appear to be reasonably accurate. The FLUKA estimate for neutron capture on  $^1\text{H}$  is  $45^{+33}_{-25}\%$  higher than the measured rate, in tension by more than  $2\sigma$ , while the Geant4 estimates agree within uncertainties. Discrepancies of the observed magnitude are common for neutron production and transport simulations. The technique of identifying neutron captures using veto-tagged data, demonstrated here, will be used in future analyses to reject  $^{137}\text{Xe}$  decays from the  $0\nu\beta\beta$  low-background dataset.

## Acknowledgments

EXO-200 is supported by DOE and NSF in the United States, NSERC in Canada, SNF in Switzerland, IBS in Korea, RFBR (14-02-00675) in Russia, DFG Cluster of Excellence ‘‘Universe’’ in Germany, and CAS-IHEP Fund and ISTCP (2015DFG02000) in China. EXO-200 data analysis and simulation uses resources of the National Energy Research Scientific Computing Center (NERSC), which is supported by the Office of Science of the U.S. Department of Energy under Contract No. DE-AC02-05CH11231. We thank Milan Krtička for his assistance with DICEBOX. The collaboration gratefully acknowledges the KARMEN Collaboration for supplying the veto detectors, and the WIPP for their hospitality.

## A Expanded table of cosmogenic nuclides of interest

Table 6 includes the nuclides expected to have the largest contribution to the  $0\nu\beta\beta$  energy ROI. Several other nuclides are also included as they may be of interest.

## B Veto-tagged data systematic effects

The normalization constraint (see published  $2\nu\beta\beta$  analysis [10] for implementation details and theory) was applied to all PDF components and serves to incorporate an overall efficiency uncertainty into the profile-likelihood fit. This 10.5% uncertainty is composed of systematic errors added in quadrature for noise tagging, 3D reconstruction efficiency, and overall efficiency. The efficiency uncertainties came from averaged rate differences between  $^{60}\text{Co}$ ,  $^{226}\text{Ra}$ , and  $^{228}\text{Th}$  source data and MC with sources deployed at several positions near the TPC. The noise tag uncertainty was evaluated by reviewing noise-tagged data events by visual inspection, looking for falsely noise-tagged valid events.

The 5.3% SS fraction constraint was based on the maximum deviation of the SS fraction determined with source data and MC among all tested sources and deployment positions. This maximum deviation was observed in  $^{228}\text{Th}$  data with source near the cathode.

All remaining systematic uncertainties were applied to the measurements after fitting, with individual uncertainties added in quadrature. These were evaluated for each capture PDF.

An additional 8% uncertainty was added separately to the  $^{136}\text{Xe}$  neutron capture detection efficiency to bring the total efficiency uncertainty to 12.5%, the maximum deviation observed in  $^{60}\text{Co}$  sum-peak data. This was motivated by the fact that  $^{136}\text{Xe}(n, \gamma)$  is a multi- $\gamma$  process, and may have systematic effects not accounted for in single- $\gamma$  source studies. A 2.5% uncertainty is added in quadrature to this to account for the effects of an observed slight shift in the energy scale for the  $^{136}\text{Xe}(n, \gamma)$  PDF, likely due to its multi- $\gamma$  nature. An additional

Region/ Nuclide	Half- life	Total energy (keV)	Decay mode	Geant4 rate (yr <sup>-1</sup> )	FLUKA rate (yr <sup>-1</sup> )
Cryostat <sup>62</sup> Co	1.5 m	5315	$\beta + \gamma$	$97.1 \pm 3.7$	$92.9 \pm 4.7$
Cryostat <sup>60</sup> Cu	24 m	6127	EC/ $\beta + \gamma$	$82.2 \pm 3.2$	$250 \pm 10$
HFE <sup>8</sup> Li	0.84 s	16004	$\beta$	$64.1 \pm 2.5$	$354 \pm 14$
HFE <sup>9</sup> Li	0.18 ms	13606	$\beta$	$8.7 \pm 0.5$	$63.0 \pm 3.6$
HFE <sup>11</sup> Be	13.8 s	11506	$\beta + \gamma$	$2.3 \pm 0.2$	$23.7 \pm 1.9$
HFE <sup>8</sup> B	0.77 s	17979	EC/ $\beta$	$5.1 \pm 0.4$	$50.3 \pm 3.1$
HFE <sup>12</sup> B	20 ms	13369	$\beta + \gamma$	$107 \pm 4$	$368 \pm 15$
HFE <sup>13</sup> B	17 ms	13437	$\beta + \gamma$	$17.6 \pm 0.8$	$79.6 \pm 4.2$
HFE <sup>15</sup> C	2.4 s	9772	$\beta + \gamma$	$146 \pm 5$	$36.3 \pm 2.5$
HFE <sup>17</sup> C	0.19 s	13166	$\beta + \gamma$	$69.6 \pm 2.7$	0.00
HFE <sup>12</sup> N	11 ms	17338	EC/ $\beta + \gamma$	$6.1 \pm 0.4$	$5.5 \pm 0.8$
HFE <sup>16</sup> N	7.1 s	10420	$\beta + \gamma$	$2380 \pm 80$	$2910 \pm 110$
HFE <sup>18</sup> N	0.62 s	13899	$\beta + \gamma$	$9.9 \pm 0.5$	$0.8 \pm 0.3$
HFE <sup>14</sup> O	71 s	5143	EC/ $\beta + \gamma$	$38.6 \pm 1.6$	$19.3 \pm 1.7$
HFE <sup>19</sup> O	27 s	4821	$\beta + \gamma$	$615 \pm 22$	$691 \pm 26$
HFE <sup>20</sup> F	11 s	7025	$\beta + \gamma$	$27490 \pm 980$	$23030 \pm 820$
TPC vessel <sup>56</sup> Co	77 d	4566	EC/ $\beta + \gamma$	$0.5 \pm 0.1$	$1.3 \pm 0.4$
TPC vessel <sup>60</sup> Co	5.3 y	2824	$\beta + \gamma$	$2.6 \pm 0.2$	$2.9 \pm 0.6$
TPC vessel <sup>62</sup> Cu	9.7 m	3948	EC/ $\beta + \gamma$	$71.7 \pm 2.8$	$76.9 \pm 4.1$
TPC LXe <sup>8</sup> Li	0.84 s	16004	$\beta$	$0.02 \pm 0.02$	$1.1 \pm 0.4$
TPC LXe <sup>108</sup> In	58 m	5157	EC/ $\beta + \gamma$	$0.14 \pm 0.05$	$0.25 \pm 0.18$
TPC LXe <sup>120</sup> I	81 m	5615	EC/ $\beta + \gamma$	$0.4 \pm 0.1$	$2.8 \pm 0.6$
TPC LXe <sup>124</sup> I	4.2 d	3160	EC/ $\beta + \gamma$	$2.5 \pm 0.2$	$8.4 \pm 1.1$
TPC LXe <sup>130</sup> I	12 h	2949	$\beta + \gamma$	$7.3 \pm 0.4$	$21.6 \pm 1.8$
TPC LXe <sup>132</sup> I	2.3 h	3577	$\beta + \gamma$	$7.7 \pm 0.5$	$22.2 \pm 1.8$
TPC LXe <sup>134</sup> I	53 m	4175	$\beta + \gamma$	$7.3 \pm 0.4$	$20.4 \pm 1.7$
TPC LXe <sup>135</sup> I	6.6 h	2648	$\beta + \gamma$	$8.6 \pm 0.5$	$21.6 \pm 1.8$
TPC LXe <sup>136</sup> I	83 s	6926	$\beta + \gamma$	$2.1 \pm 0.2$	$1.7 \pm 0.5$
TPC LXe <sup>121</sup> Xe	40 m	3745	EC/ $\beta + \gamma$	$0.6 \pm 0.1$	$1.0 \pm 0.4$
TPC LXe <sup>135</sup> Xe	9.1 h	1151	$\beta + \gamma$	$1110 \pm 40$	$1060 \pm 40$
TPC LXe <sup>137</sup> Xe	3.8 m	4173	$\beta + \gamma$	$439 \pm 17$	$403 \pm 16$

**Table 6.** Expanded table of cosmogenic radionuclides of interest. The half-lives, decay mode, and total decay energy are listed [53]. The Geant4 and FLUKA columns give the estimated production rate for the listed nuclide in atoms per year. Uncertainties are dominated by muon flux and MC statistics.

cascade model uncertainty was applied for the <sup>136</sup>Xe capture as well. The cascade model uncertainty evaluation is described in section 3.3.

The efficiency to detect captures depends strongly on their position distribution. The relative number of captures calculated by FLUKA on each degenerate component (such as the concentric shells of HFE-7000) was assumed to be our most accurate estimate. To account for uncertainties in the modeling of capture positions among degenerate components, differences in average capture  $\gamma$  detection efficiency resulting from the capture position distributions



obtained from FLUKA and Geant4 were treated as a systematic uncertainty. Deviations in the fitted degenerate PDF ratios from their simulation values were evaluated to add to this position uncertainty. To account for non-uniform captures within each component (within a single shell of HFE, for example), the Geant4 capture positions were used to determine a small correction, which was applied for all efficiencies.

The probability for each type of capture to be coincident with a veto panel trigger was estimated from FLUKA simulation. These raw simulated efficiencies were scaled by a factor of 0.983, necessary to bring the 97.99% FLUKA efficiency for TPC muons to be tagged by veto panels in line with the  $96.35 \pm 0.11\%$  value determined from the full data set. This need for a correction was attributed to the lack of response modeling of the veto detectors in simulation. Although corrected for, we treated this efficiency scaling as an additional uncertainty.

Several contributions to the total efficiency depend on the time distribution of neutron captures. The following effects were considered: capture time window ( $10 \mu\text{s} - 5 \text{ms}$ ), reduced reconstruction efficiency following a TPC muon, reduced reconstruction efficiency following another capture event, drift time cut ( $119 \mu\text{s}$  between scintillation events), and reduced efficiency at the edges of the data frame. Models for these efficiencies were developed based on radioactive source data and other data. The capture efficiencies were estimated by applying these models (with the exception of the frame edge efficiency, applied separately) to the FLUKA simulated capture events. We chose the FLUKA simulation for this because it replicated the observed capture time distribution better than Geant4. Agreement between the FLUKA expected capture times and data was tested by fitting capture times with an exponential and comparing data and MC. Optimal agreement was found by scaling the FLUKA capture times by a factor of 1.05, so this is applied for all FLUKA capture time studies. Plots of the FLUKA capture time distribution and the aforementioned efficiencies are shown in figure 12.

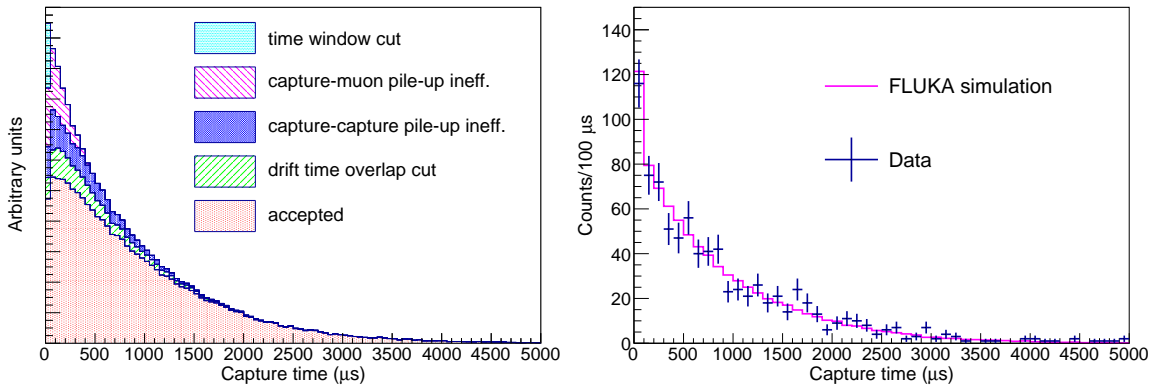


**Figure 12.** (left) Distribution of the observed capture times (time since muon) for neutrons on  $^1\text{H}$  in HFE-7000, as estimated from FLUKA simulation. Each of the timing cuts and efficiencies (except the frame edge efficiency) are applied, reducing the total efficiency for observing these captures. (right) FLUKA distribution for observed capture times for all veto-tagged events, after time-dependent efficiencies are applied. Data from veto-tagged events are overlaid in blue, and the number of MC counts is scaled to match the data. In both panels, the FLUKA capture times have been scaled by 1.05.

The capture time window cut and drift time cuts were applied to the FLUKA simulation in a straightforward manner. The muon-capture pile-up inefficiency was evaluated and

parameterized based on veto-tagged data. Our reconstruction algorithms are optimized for isolated scintillation clusters, and are less sensitive to signals occurring within several hundred  $\mu\text{s}$  after the large muon signal. These capture signals can still be identified with simple thresholding technique, at the expense of energy and timing precision. We search for missed scintillation clusters using this technique, thus finding the fraction of captures missed as a function of time since TPC muon.

The reconstruction efficiency dips for any scintillation clusters too near each other in time (capture-capture pile-up), and for scintillation clusters at the beginning and end of the 2048  $\mu\text{s}$  data frame (frame-edge effects). These were quantified using source data. The deficit in the time between events ( $\Delta t$ ) distribution at small  $\Delta t$  in source data provides a measure of signal loss. The fraction of counts at the beginning and end of a frame to be lost in source data was used to quantify the frame edge timing loss. See figure 13 for examples. All events with scintillation clusters within 120  $\mu\text{s}$  of the end of a frame are not used for analysis (as charge clusters may be lost if their collection signal waveforms are not completed by the end of the frame), but we used the number of observed veto-tagged counts in this time to extrapolate, using the source data efficiency, to the number of events lost at the end of data frames. The number of events lost at the beginning of data frames was related to the number lost at the end based on the source data studies. This extrapolation yielded a  $97.1 \pm 1.6\%$  data frame efficiency, which was applied to all PDFs.

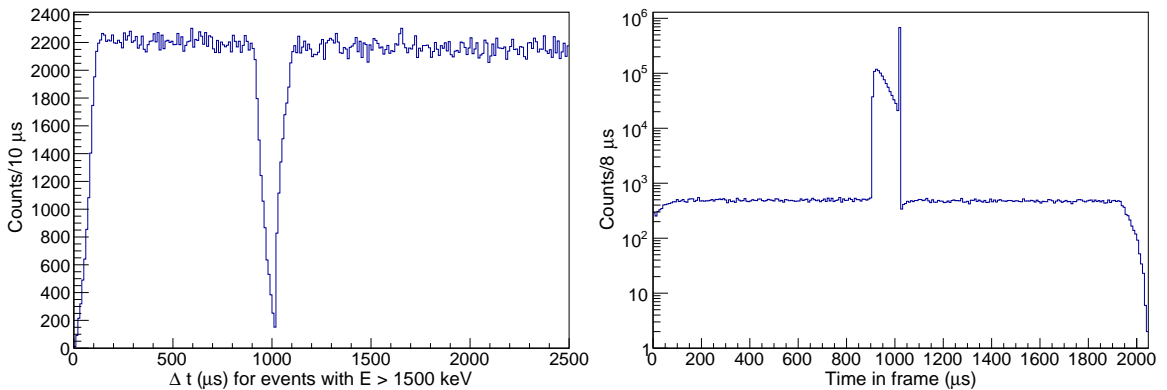


**Figure 13.** Examples of source studies for timing-based efficiency. On the left is the distribution of events as a function of  $\Delta t$ , time since the previous event, for data from a  $^{228}\text{Th}$  source deployed at a position near the cathode (designated “S5”). The deficit at short times was fitted, and the resulting efficiency as a function of  $\Delta t$  was applied to the FLUKA MC to incorporate this effect. The scintillation cluster-finding algorithm is optimized for isolated clusters, and does not perform well when scintillation events occur in quick succession. The deficit near 1024  $\mu\text{s}$  is due to inefficiencies for reconstructing signals at the very end or very beginning of a data frame, and this effect is explored in more detail in the right panel. The right panel shows the distribution of scintillation cluster times in the 2 ms data frame for  $^{226}\text{Ra}$  data at S5. The DAQ software records the data such that the trigger is set to 1024  $\mu\text{s}$ , so the sharp peak and broad peak in the feature near the frame center are due to triggers on scintillation light and charge, respectively. The flat part of the distribution is due to pile-up. The deficits at the beginning and end of the frame are fitted and used to estimate rates of event loss due to frame-edge effects. Several different source positions needed to be used as the frame-edge efficiency is highly dependent on the time for charge deposits to drift to the anode. In both cases, only events with  $E > 1500$  keV are considered.

After these reconstruction efficiencies were introduced to the FLUKA MC, calculated

efficiencies for each PDF were evaluated. All timing efficiencies came directly from this modified FLUKA MC, except for the drift time cut efficiency and frame-edge efficiency. The capture-capture pile-up efficiency has no effect on total efficiency after the drift time cut is applied. For the drift time cut, FLUKA estimated an overall efficiency of 89.5% for veto-tagged events, while data showed a 94.6% efficiency (after correction for the capture-capture pile-up inefficiency). To account for this discrepancy, a scale factor for this inefficiency of  $0.75 \pm 0.37$  was applied to the inefficiency for each PDF, yielding an adjusted overall drift time cut efficiency of  $92.1 \pm 3.9\%$ , in agreement within uncertainties with the efficiencies from both data and MC. The capture-capture pile-up efficiency (average 89.9% for all data) was then added in, yielding a final average efficiency of  $82.8 \pm 6.4\%$ .

The uncertainty for the time window efficiency was set to the maximum difference between Geant4 and FLUKA calculations (with and without time scaling factors). The uncertainty for TPC muon-induced inefficiency was conservatively set to the entirety of the correction, and the frame edge efficiency uncertainty was based on differences between different source position results.

## References

- [1] **KamLAND-Zen** Collaboration, A. Gando et al., *Limit on Neutrinoless  $\beta\beta$  Decay of  $^{136}\text{Xe}$  from the First Phase of KamLAND-Zen and Comparison with the Positive Claim in  $^{76}\text{Ge}$* , *Phys. Rev. Lett.* **110** (2013) 062502, [[arXiv:1211.3863](#)].
- [2] **EXO-200** Collaboration, J. B. Albert et al., *Search for Majorana neutrinos with the first two years of EXO-200 data*, *Nature* **510** (2014) 229, [[arXiv:1402.6956](#)].
- [3] **GERDA** Collaboration, M. Agostini et al., *Results on Neutrinoless Double- $\beta$  Decay of  $^{76}\text{Ge}$  from Phase I of the GERDA Experiment*, *Phys. Rev. Lett.* **111** (2013) 122503, [[arXiv:1307.4720](#)].
- [4] **EXO-200** Collaboration, M. Auger et al., *The EXO-200 detector, part I: Detector design and construction*, *JINST* **7** (2012) P05010, [[arXiv:1202.2192](#)].
- [5] M. Redshaw, E. Wingfield, J. McDaniel, and E. G. Myers, *Mass and double-beta-decay  $Q$  value of  $\text{Xe-136}$* , *Phys. Rev. Lett.* **98** (2007) 053003.
- [6] 3M Novec 7000 Engineered Fluid (HFE-7000), <http://www.3m.com>.
- [7] H. Gemmeke et al., *The High resolution neutrino calorimeter KARMEN*, *Nucl. Instrum. Meth.* **A289** (1990) 490.
- [8] **EXO-200** Collaboration, J. B. Albert et al., *Measurements of the ion fraction and mobility of  $\alpha$ - and  $\beta$ -decay products in liquid xenon using the EXO-200 detector*, *Phys. Rev. C* **92** (2015) 045504, [[arXiv:1506.00317](#)].
- [9] **EXO-200** Collaboration, J. B. Albert et al., *Investigation of radioactivity-induced backgrounds in EXO-200*, *Phys. Rev.* **C92** (2015) 015503, [[arXiv:1503.06241](#)].
- [10] **EXO-200** Collaboration, J. B. Albert et al., *Improved measurement of the  $2\nu\beta\beta$  half-life of  $^{136}\text{Xe}$  with the EXO-200 detector*, *Phys. Rev.* **C89** (2014) 015502, [[arXiv:1306.6106](#)].
- [11] G. C. Carlson, W. C. Schick Jr., W. L. Talbert Jr., and F. K. Wohn, *Half-lives of some short-lived mass-separated gaseous fission products and their daughters*, *Nuclear Physics A* **125** (1969) 267.
- [12] R. J. Onega and W. W. Pratt, *Decay of  $\text{Xe}^{137}$* , *Phys. Rev.* **136** (1964) B365.

- [13] E. Browne and J. K. Tuli, *Nuclear Data Sheets for  $A = 137$* , *Nuclear Data Sheets* **108** (2007) 2173. Data extracted from the ENSDF database, version February 12, 2015, <http://www.nndc.bnl.gov/>.
- [14] J. Allison et al., *Geant4 developments and applications*, *IEEE Trans. Nucl. Sci.* **53** (2006) 270.
- [15] **GEANT4** Collaboration, S. Agostinelli et al., *GEANT4: A Simulation toolkit*, *Nucl. Instrum. Meth.* **A506** (2003) 250.
- [16] **Particle Data Group** Collaboration, K. A. Olive et al., *Review of Particle Physics*, *Chin. Phys.* **C38** (2014) 090001.
- [17] S. Miyake, *Rapporteur Paper on Muons and Neutrinos*, in *Proceedings of the 13th International Cosmic Ray Conference*, vol. 5, p. 3638, 1973.
- [18] D. Mei and A. Hime, *Muon-induced background study for underground laboratories*, *Phys. Rev.* **D73** (2006) 053004, [[astro-ph/0512125](https://arxiv.org/abs/astro-ph/0512125)].
- [19] E.-I. Esch et al., *The Cosmic ray muon flux at WIPP*, *Nucl. Instrum. Meth.* **A538** (2005) 516, [[astro-ph/0408486](https://arxiv.org/abs/astro-ph/0408486)].
- [20] R. O. Duda and P. E. Hart, *Use of the Hough transformation to detect lines and curves in pictures*, *Commun. ACM* **15** (1972) 11.
- [21] S. Herrin, *Double Beta Decay in Xenon-136: Measuring the Neutrino-Emitting Mode and Searching for Majoron-Emitting Modes*. PhD thesis, Stanford U., Phys. Dept., 2013. Appendix A.
- [22] T. Gaisser and T. Stanev, *Muon Bundles in Underground Detectors*, *Nucl. Instrum. Meth.* **A235** (1985) 183.
- [23] T. M. Cannon and R. O. Stenerson, *Multiple muons deep underground*, *J. Phys.* **A4** (1971) 266.
- [24] G. L. Cassiday, J. W. Keuffel, and J. A. Thompson, *Calculation of the stopping-muon rate underground*, *Phys. Rev.* **D7** (1973) 2022.
- [25] M. Crouch, *An Improved World Survey Expression for Cosmic Ray Vertical Intensity vs. Depth in Standard Rock*, *International Cosmic Ray Conference* **6** (1987) 165.
- [26] T. Böhlen, F. Cerutti, M. Chin, A. Fassò, A. Ferrari, P. Ortega, A. Mairani, P. Sala, G. Smirnov, and V. Vlachoudis, *The FLUKA code: Developments and challenges for high energy and medical applications*, *Nuclear Data Sheets* **120** (2014) 211 – 214.
- [27] A. Ferrari, P. R. Sala, A. Fassò, and J. Ranft, *FLUKA: A multi-particle transport code*, *CERN-2005-010, SLAC-R-773, INFN-TC-05-11* (2005).
- [28] K. L. Kuhlman and B. Malama, *Brine flow in heated geologic salt*, Tech. Rep. SAND2013-1944, Sandia National Laboratories, Mar, 2013.
- [29] H. Sorge, H. Stoecker, and W. Greiner, *Poincare Invariant Hamiltonian Dynamics: Modeling Multi - Hadronic Interactions in a Phase Space Approach*, *Annals Phys.* **192** (1989) 266.
- [30] S. Roesler, R. Engel, and J. Ranft, *The Monte Carlo event generator DPMJET-III*, [[hep-ph/0012252](https://arxiv.org/abs/hep-ph/0012252)].
- [31] Geant4, “Bugzilla/Geant4 - Problem 1680: photonuclear production cross section at giant dipole resonance wrong by factor 3.” [http://bugzilla-geant4.kek.jp/show\\_bug.cgi?id=1680](http://bugzilla-geant4.kek.jp/show_bug.cgi?id=1680).
- [32] D. R. Tilley, H. R. Weller, and C. M. Cheves, *Energy levels of light nuclei  $A = 16-17$* , *Nucl. Phys.* **A564** (1993) 1.
- [33] E. Browne and J. Tuli, *Nuclear Data Sheets for  $A = 60$* , *Nuclear Data Sheets* **114** (2013) 1849.
- [34] B. Singh, *Nuclear Data Sheets for  $A = 130$* , *Nuclear Data Sheets* **93** (2001) 33.

- [35] Y. Khazov, A. Rodionov, S. Sakharov, and B. Singh, *Nuclear Data Sheets for  $A = 132$* , *Nuclear Data Sheets* **104** (2005) 497.
- [36] A. Sonzogni, *Nuclear Data Sheets for  $A = 134$* , *Nuclear Data Sheets* **103** (2004) 1.
- [37] B. Singh, A. A. Rodionov, and Y. L. Khazov, *Nuclear Data Sheets for  $A = 135$* , *Nuclear Data Sheets* **109** (2008) 517.
- [38] S. Mughabghab, *Atlas of Neutron Resonances: Resonance Parameters and Thermal Cross Sections.  $Z=1-100$* . Elsevier Science, 2006.
- [39] S. G. Prussin, R. G. Lanier, G. L. Struble, L. G. Mann, and S. M. Schoenung, *Gamma rays from thermal neutron capture in Xe-136*, *Phys. Rev.* **C16** (1977) 1001.
- [40] F. Bečvář, *Simulation of  $\gamma$  cascades in complex nuclei with emphasis on assessment of uncertainties of cascade-related quantities*, *Nucl. Instrum. Meth.* **A417** (1998) 434.
- [41] B. Singh, *Nuclear Data Sheets for  $A = 64$* , *Nuclear Data Sheets* **108** (2007) 197. Data extracted from the ENSDF database, version July 7, 2013, <http://www.nndc.bnl.gov/>.
- [42] E. Browne and J. K. Tuli, *Nuclear Data Sheets for  $A = 66$* , *Nuclear Data Sheets* **111** (2010) 1093. Data extracted from the ENSDF database, version July 7, 2013, <http://www.nndc.bnl.gov/>.
- [43] J. K. Tuli, *Evaluated nuclear structure data file: A Manual for Preparation of Data Sets*, Tech. Rep. BNL-NCS-51655-01/02 Rev., Brookhaven National Laboratory, 2001.
- [44] D. Tilley, C. Cheves, J. Kelley, S. Raman, and H. Weller, *Energy levels of light nuclei,  $A = 20$* , *Nuclear Physics A* **636** (1998) 249. Data extracted from the ENSDF database, version February 12, 2015, <http://www.nndc.bnl.gov/>.
- [45] A. Fassò, A. Ferrari, P. Sala, and G. Tsiledakis, *Implementation of Xenon Capture Gammas in FLUKA for TRD Background Calculations*, in *Proceedings of the Sixth Meeting of the Task Force on Shielding Aspects of Accelerators, Targets and Irradiation Facilities*, pp. 397–406, NEA, Apr., 2002.
- [46] S. Wilks, *The Large-Sample Distribution of the Likelihood Ratio for Testing Composite Hypotheses*, *Annals Math. Statist.* **9** (1938) 60.
- [47] G. Cowan, *Statistical data analysis*. Oxford Science Publications. Clarendon, 1998.
- [48] **KamLAND** Collaboration, S. Abe et al., *Production of Radioactive Isotopes through Cosmic Muon Spallation in KamLAND*, *Phys. Rev.* **C81** (2010) 025807, [[arXiv:0907.0066](https://arxiv.org/abs/0907.0066)].
- [49] L. Reichhart et al., *Measurement and simulation of the muon-induced neutron yield in lead*, *Astropart. Phys.* **47** (2013) 67, [[arXiv:1302.4275](https://arxiv.org/abs/1302.4275)].
- [50] M. G. Marino, J. A. Detwiler, R. Henning, R. A. Johnson, A. G. Schubert, and J. F. Wilkerson, *Validation of spallation neutron production and propagation within Geant4*, *Nucl. Instrum. Meth.* **A582** (2007) 611, [[arXiv:0708.0848](https://arxiv.org/abs/0708.0848)].
- [51] **Borexino** Collaboration, G. Bellini et al., *Cosmogenic Backgrounds in Borexino at 3800 m water-equivalent depth*, *JCAP* **1308** (2013) 049, [[arXiv:1304.7381](https://arxiv.org/abs/1304.7381)].
- [52] W. B. Wilson, *SOURCES 4A : a code for calculating ( $\alpha, n$ ) spontaneous fission, and delayed neutron sources and spectra*, Tech. Rep. LA-13639-MS, Los Alamos National Laboratory, Los Alamos, NM, USA, 1999.
- [53] R. B. Firestone, C. Baglin, and S. Y. F. Chu, *Table of isotopes: 1998 update with CD-ROM*. Wiley, New York, NY, 1998.